Tropical cyclone formation regions in CMIP5 models: a global performance assessment and projected changes

K. J. Tory[1] · H. Ye[1] · G. Brunet[1]

Abstract

Tropical Cyclone (TC) formation regions are analysed in twelve CMIP5 models using a recently developed diagnostic that provides a model-performance summary in a single image for the mid-summer TC season. A subjective assessment provides an indication of how well the models perform in each TC basin throughout the globe, and which basins can be used to determine possible changes in TC formation regions in a warmer climate. The analysis is necessarily succinct so that seven basins in twelve models can be examined. Consequently, basin performance was reduced to an assessment of two common problems specific to each basin. Basins that were not too adversely affected were included in the projection exercise. The North Indian basin was excluded because the mid-summer analysis period covers a lull in TC activity. Surprisingly, the North Atlantic basin also had to be excluded, because all twelve models failed the performance assessment. A slight poleward expansion in the western North Pacific and an expansion towards the Hawaiian Islands in the eastern North Pacific is plausible in the future, while a contraction in the TC formation regions in the eastern South Indian and western South Pacific basins would reduce the Australian region TC formation area. More than half the models were too active in the eastern South Pacific and South Atlantic basins. However, projections based on the remaining models suggest these basins will remain hostile for TC formation in the future. These southern hemisphere changes are consistent with existing projections of fewer southern hemisphere TCs in a future warming world

1 Introduction

Projections of fewer tropical cyclones (TC) globally in a warming world have been consistent for more than a decade now (e.g., Knutson et al. 2010, 2019; Walsh et al. 2015). However, most global coupled ocean–atmosphere climate models continue to struggle to reproduce realistic TC climatologies in some basins, including the very active North Atlantic basin, which casts doubt on any projections made for these specific basins. Confidence in projections can be improved if it can be established how realistic model TC formation is, and if we can understand why TC formation climatologies change between future and present-day scenarios (Tory et al. 2018, hereafter T18). In order to answer these questions T18 sought to identify a set of basic parameters that define where TCs can and cannot form (TC formation boundaries) and identify fundamental atmospheric

and oceanic climate circulations that determine the global distribution of these parameters. In this paper the T18 TC formation boundary parameters are applied to a selection of Phase 5 of the Coupled Model Intercomparison Project (CMIP5, Taylor et al. 2012) models during the peak summer TC seasons (i.e., January to March, southern hemisphere, July to September, northern hemisphere), to provide insight into why the models produce TCs where they do. The results are used to determine subjectively which models, and basins within models, can be used to make projections of plausible future changes in peak-season TC formation regions. For brevity this paper only provides a general overview of global results.

In the next section the TC detection and TC formation boundary methodologies are described, and the choice of CMIP5 models investigated explained. In Sect. 3, model performance for each TC basin is presented and discussed. In Sect. 4, plausible future scenarios are proposed for most TC basins based on model basins that were reported to perform well in Sect. 3. A summary is provided in Sect. 5.

✉ K. J. Tory
   kevin.tory@bom.gov.au

1   Bureau of Meteorology, GPO Box 1289, Melbourne,
    VIC 3001, Australia

2 Methods

The tropical depression (TD) and tropical Storm (TS) detection algorithm, and the TC formation boundary analysis of T18, are applied to twelve CMIP5 models forced under the historical (years 1970—2000) and Representative Concentration Pathway 8.5 (RCP8.5, years 2070—2100[1]) conditions. The development and application of the Okubo-Weiss Zeta Paramater (OWZP) TS detection algorithm has been documented in a series of papers (Tory et al. 2013a, b, c, d; Tory and Dare 2015) and summarised most recently in T18, where an adjustment to the methodology to detect TDs is also described. T18 also describes the development of the TC formation boundary diagnostic in detail. Brief summaries are provided in the following subsections.

T18 used 34 years of ERA-Interim data to identify TC formation boundaries during the most climatically stable months of January—March and July—September for the southern and northern hemispheres, respectively. The boundaries were "tuned" to a TC formation "truth" provided by TS and TD detections for the same period. Detections rather than observed TCs were chosen for the "truth" to ensure the formation boundaries were globally consistent (the inclusion of weaker TCs in observed databases are not consistent in time or between basins), and to maximise consistency between TCs and formation boundaries when applied to climate models.

2.1 TD and TS detections

The OWZP tropical cyclone detection algorithm identifies atmospheric circulations that are ripe for TC formation. If the specified conditions remain favourable for a continuous 24 (48) hours a TD (TS) is assumed to have formed. Note, by definition all TSs were once TDs, so only those TDs that failed to develop further to TS intensity are described as TDs in this paper. The conditions require a rotating, moist environment extending from the low- to mid-troposphere, with low to moderate shear. The conditions are determined by a set of parameter thresholds that must be met on at least two neighbouring grid-points after the model native grid has been interpolated to a standard 1° by 1° latitude, longitude grid. A variant of the Okubo–Weiss parameter (OWZ) on 850 and 500 hPa pressure levels is used to determine sufficient rotation, and 950 and 700 hPa relative humidity and 950 specific humidity thresholds determine sufficient moisture. A threshold of the difference in vector winds between 850 and 200 hPa eliminates environments with excessive shear.

2.2 Formation boundary thresholds

T18 tested many dynamic and thermodynamic parameters with the aim to define global regions of TC formation using a minimum number of threshold quantities. This is illustrated for the summer months in Fig. 1. The equatorial boundary was largely defined by a composite parameter representing the ratio of 850 hPa absolute vorticity (η_{850}) to the meridional gradient of absolute vorticity at 700 hPa ($\beta_{700}^* = \frac{\partial \eta}{\partial y}$),

$$\xi = \frac{|\eta|_{850}}{\beta_{700}^*(R/2\Omega)} = 2 \times 10^{-5} s^{-1} \tag{1}$$

Here R and Ω, the earth radius and rotation frequency, normalise β^* to give ξ the same units as η. The η magnitude is used to ensure ξ is positive in both hemispheres. No physical explanation was provided in T18 for why ξ should provide such a good equatorward TC formation boundary. Equation 1 is similar to an index introduced in Brunet and Haynes (1995) that essentially determines if a disturbance in a shear flow will roll-up into a vortex or be sheared apart. We tested a modified version of ξ, roughly equivalent to the Brunet and Haynes (1995) index,

$$\xi_{mod} = \frac{|\eta|_{850}}{\left[\beta_{700}^*(R/2\Omega)\right]^2} = 1.7 \times 10^{-5} s^{-1} \tag{2}$$

which was found to perform as well as Eq. 1, due to large gradients in both β^* and η. The Brunet and Haynes (1995) index is roughly equivalent to $\frac{\sqrt{|\eta|}}{\beta^*}$, where the numerator represents disturbance amplitude and the denominator the destructive potential of the shear flow. Using this index, Asaadi et al. (2016, 2017) demonstrated that the coexistence of a nonlinear critical layer and a region of weak meridional Potential Vorticity (PV) gradient over several days, is likely to be necessary for easterly waves to develop into named storms, and seems to explain the well-known fact that only about one quarter of African easterly waves contribute to tropical cyclogenesis. In this paper we continue to use Eq. 1 but note that either equation could be used.

T18 imposed a limit to the denominator of Eq. 1 ($\beta_{700}^* \geq 5 \times 10^{-12} m^{-1} s^{-1}$). In the current paper an additional limit is applied to the numerator ($|\eta|_{850} \geq 1.75 \times 10^{-5} s^{-1}$). This limit was inspired by the insight gained from Brunet and Haynes (1995), which suggested small values of β^* might allow a weak disturbance to roll up into a vortex, but it could take an unrealistically long time, suggesting a limit on the disturbance amplitude (here, the absolute vorticity) would be required. The value chosen is less than the $|\eta|_{850}$ thresholds tested by T18.

---

[1] Three models, do not have data for the year 2100 (BC1, BCM and HG2). For these models the years 2069—2099 are used instead.
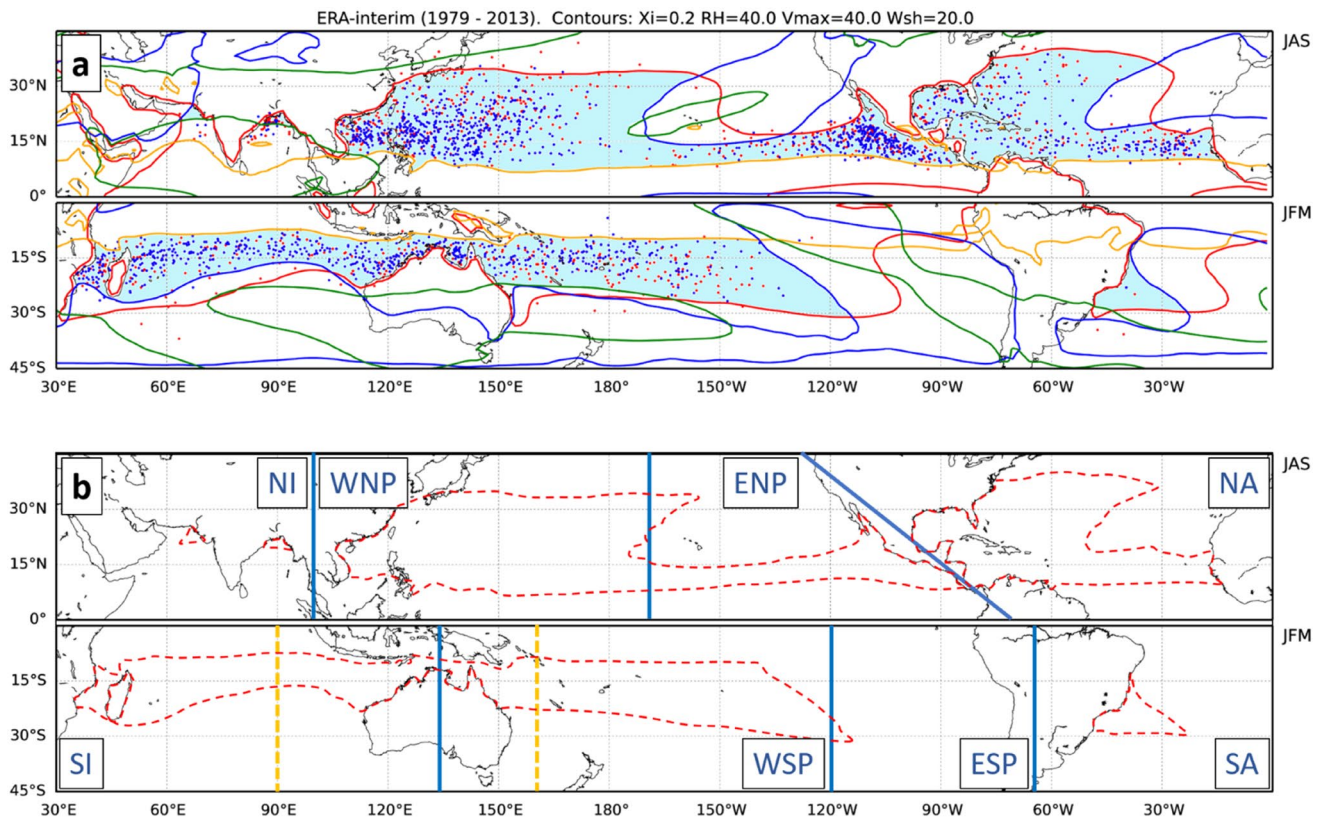
Fig. 1 **a** ERA-Interim global TC formation regions (shaded) for the summer months (July—September, northern hemisphere, and January—March, southern hemisphere) as defined by the TC formation boundaries: $\xi = 2 \times 10^{-5} s^{-1}$ (orange), $V_{PI} = 40 ms^{-1}$ (red), $RH_{700} = 40\%$ (blue) and $V_{sh} = 20 ms^{-1}$ (green). OWZP detected TCs exceeding TS intensity (blue dots) and TDs that did not become TSs (red dots) are overlaid. See text for acronym and symbol definitions. **b** Blue lines mark the intersection of the TC formation basins, labelled with basin name abbreviations listed in Table 1. The Australian region, discussed in the text, lies between the yellow dashed lines. The ERA-Interim TC formation regions are outlined by red dashed lines

The poleward boundaries are mostly defined by Emanuel's (e.g., Bister and Emanuel 2002) maximum potential intensity,

$$V_{PI} = 40 \, \text{ms}^{-1} \tag{3}$$

and 700 hPa relative humidity,

$$RH_{700} = 40\% \tag{4}$$

The addition of a windshear threshold was required to eliminate mid-summer formation in the North-Indian ocean basin, and winter formation in large parts of the northern hemisphere ITCZ,

$$V_{sh} = \sqrt{\left(u_{200} - u_{850}\right)^2 + \left(v_{200} - v_{850}\right)^2} = 20 \, \text{ms}^{-1} \tag{5}$$

2.3 Formation boundaries in ERA-Interim

The TC formation boundaries applied to ERA-Interim data (Fig. 1) provide insight into how global atmospheric and oceanic circulations affect TC formation. The favourable formation regions are in general thinner in the east of each ocean basin compared with the west but are otherwise unique to each ocean and hemisphere. (Table 1 lists the ocean basin name acronyms depicted in Fig. 1b and used throughout the paper.) The patterns are unique since they are dominated by ocean currents, which are shaped by the distribution of continental land masses and prevailing winds (See the Comet Project: https://ftp.comet.ucar.edu/ootw/tropical/textbook_2nd_edition/navmenu.php_tab_4_page_0.0.0.htm). Oceanic anticyclones transport cooler upwelling water equatorward in the east and transport warmer water poleward in the west of each basin except the North Indian (NI) where the anticyclone is inhibited by the Asian continent. This pattern is evident in the V_{PI} boundaries (red contours), given the strong influence of SST on V_{PI}. Lower troposphere atmospheric anticyclones (comprising easterly trade winds and midlatitude westerly winds) impact the humidity in a similar way, with dry air advected equatorward and westward in the eastern ocean basins, and moist air advected poleward in the western ocean basins, as indicated

Table 1 Names and codes for the TC ocean basins depicted in Fig. 1b, featured in Tables 4, 5, 6 and 7, and discussed throughout the text

Basin name	Basin code
North Indian	NI
Western North Pacific	WNP
Eastern North Pacific	ENP
North Atlantic	NA
South Indian	SI
Western South Pacific	WSP
Australian	Aus
Eastern South Pacific	ESP
South Atlantic	SA

by the RH_{700} boundaries (blue contours). Cross-equatorial flow in the summer months pushes the ξ boundary poleward (orange contours) ensuring low-latitude formation is a rare occurrence, and as mentioned above, wind shear (green contours) plays a secondary role in the summer months except in NI basin, where shear associated with the monsoon is excessive.

Applying the foregoing TC formation boundary thresholds to CMIP5 models, we use the pattern and position of each threshold quantity to diagnose how well the atmospheric/oceanic circulations relevant to TC formation are represented in each model, and the impact this has on model TC formation.

2.4 CMIP5 models

Our research group originally analysed 20 CMIP5 models for TC formation using the OWZP TC detector (e.g., Tory et al. 2014). Seven of these models were rejected for producing too few TCs (less than one third of observed TC numbers) and one (MRI-CGCM3)[2] for producing more than double the observed number (Table 2). In the current study the same eight models are rejected. Table 2 suggests that low resolution likely impacts a model's ability to generate a realistic global TC climatology (as defined by the OWZP TC detection scheme). However, the two BCC models are exceptions that illustrate resolution alone does not determine

---

[2] In order to satisfy our curiosity regarding why the MRI-CGCM3 model was over-active, we applied the TC formation boundary analysis to the historical scenario and found the atmosphere to be overly humid. This is likely responsible for the high formation densities. It also broadened most TC formation basins poleward, providing larger geographic areas favourable for TC formation (not shown). Interestingly, Bell et al. (2020b) found that removing short-lived TCs (OWZ-detections) from their MRI-CGCM3 analysis gave a reasonable climatology.

TC frequency. Projections are based on differences between the CMIP5 historical (1970—2000) and rcp85 (2070—2100) scenarios.

The development of the TC formation boundary methodology using ERA-Interim data biases the results to the specific atmosphere–ocean model used in that analysis. The different resolutions and model physics in the CMIP5 models could mean the TC formation boundary thresholds set in T18 are not ideal in the climate models, which justifies limited retuning of thresholds. Table 3 lists the retuned thresholds, plus three-character model-name abbreviations used throughout the paper. Subjective threshold changes were applied to adjust the boundaries to better match the TC detections. A relaxation of the ξ threshold was applied to the medium- and low-resolution models. This was necessary because the double derivatives inherent in ξ smear out the parameter when applied to coarser resolution models, which leads to a poleward drift of the T18 threshold location. The higher resolution models required no adjustment to the V_{PI} and V_{sh} thresholds, although a slight relaxing of the MI5 V_{sh} threshold was introduced to better include a region of frequent formation in the NI basin. The V_{sh} threshold was relaxed in four other models (Table 3) for the same reason, plus it provided improvements to the WNP basin (see later sections). Changes to the RH_{700} thresholds appear to be resolution independent, with both high- and medium-resolution models seeing thresholds reduced to 35% necessary to better represent the eastern SI basin and eastern NA basin. A more drastic reduction of the RH_{700} threshold was required in CN5, which suggests the model may have a dry bias, and may explain relatively low annual TS numbers (despite relatively high model resolution, Table 2). Finally, small increases in V_{PI} thresholds for GFG and GFM, and for CSI a decrease in the V_{PI} and an increase in the RH_{700} thresholds, provided modest improvements in most basins.

To minimize repetition in the upcoming sections, a subset of four models are chosen to focus the discussion, before drawing comparisons with the remaining models. To capture the influence of model resolution we choose to include in the subset the highest (BCM) and lowest (BC1) resolution models, and two medium resolution models that represent the diversity of model performance (AC0 and GF3). The figure subplot labels are in red for these four models in Figs. 2, 3, 4 for easy identification. In choosing the four models the interdependency between models (e.g., Knutti et al. 2013) was considered. To investigate resolution dependency, it is beneficial for the models to come from the same family, whereas, to illustrate diversity the remaining two models were chosen from separate model families. There are three model families in the models used in this study (indicated in the last column of Table 3) plus four unrelated models. The BCC family includes two models from the Beijing Climate Center. The GFDL family includes three models from the

Table 2 Model details

Model	lon × lat	20th C	21st C	% Δ	References
IBTrACS (Obs)		76.2			The International Best Track Archive for Climate Stewardship (IBTrACS, Knapp et al. 2010)
MRI-CGCM3	320 × 160	155.2	126.8	− 18.30	Meteorological Research Institute, Japan Yukimoto et al. (2012)
BCC-CSM1-1-m	**320 × 160**	**68.6**	**73.9**	**7.73**	Beijing Climate Centre (BCC), these models are based on NCAR CCSM2.0.1 (Wu et al. 2014)
CCSM4	**288 × 192**	**57.1**	**52.3**	**− 8.41**	National Center for Atmospheric Research (NCAR) Gent et al. (2011)
CNRM-CM5	**256 × 128**	**48.5**	**44.2**	**− 8.87**	Centre National de Recherches Météorologiques (CNRM) Voldoire et al. (2012)
MIROC5	**256 × 128**	**111.3**	**86.3**	**− 22.46**	Model of Interdisciplinary Research on Climate (MIROC) Watanabe et al. (2010)
ACCESS1-0	**192 × 144**	**74.9**	**63.5**	**− 15.22**	Bureau of Meteorology (BoM) the Australian Community Climate and Earth-System Simulator (ACCESS) models are based on the UK Met Office's Unified Model Bi et al. (2012)
ACCESS1-3	**192 × 144**	**89.7**	**80.8**	**− 9.92**	
HadGEM2-ES	**192 × 144**	**97.5**	**82.7**	**− 15.18**	HadGEM2-ES is a configuration of the UK Met Office's Unified Model Jones et al. (2011)
CSIRO-Mk3.6.0	**192 × 96**	**101.2**	**89.7**	**− 11.36**	Commonwealth Scientific and Industrial Research Organization (CSIRO) Collier et al. (2011)
IPSL-CM5A-MR	144 × 143	18.0	30.7	70.56	Institute Pierre Simon Laplace Dufresne et al. (2013)
NorESM1M	144 × 96	20.1	17.6	− 12.44	Research Council of Norway—Norwegian Climate Centre Bentsen et al. (2012)
GFDL-CM3	**144 × 90**	**85.2**	**61.7**	**− 27.58**	Geophysical Fluid Dynamics Laboratory (GFDL) (Donner et al. 2011)
GFDL-ESM2M	**144 × 90**	**82.5**	**76.9**	**− 6.79**	
GFDL-ESM2G	**144 × 90**	**85.6**	**77.6**	**− 9.35**	
CanESM2	128 × 64	14.1	15.6	10.64	Canadian Centre for Climate Modelling and Analysis
MIROC-ESM	128 × 64	13.4	10.3	− 23.13	Model of Interdisciplinary Research on Climate (MIROC) Watanabe et al. (2011)
MIROC-ESM-CHEM	128 × 64	12.6	10.7	− 15.08	
BCC-CSM1.1	**128 × 64**	**76.7**	**67.6**	**− 11.86**	Beijing Climate Centre (BCC), these models are based on NCAR CCSM2.0.1 Wu et al. (2014)
FGOALS-g2	128 × 60	21.5	31.0	44.19	State Key Laboratory of Numerical Modeling for Atmospheric Sciences and Geophysical Fluid Dynamics, Center for Earth System Science, China Zhou et al. (2018)
IPSL-CM5A-LR	96 × 96	7.5	14.1	88.00	Institute Pierre Simon Laplace Dufresne et al. (2013)

Row 1 contains observed global annual Tropical Storm counts. The remaining rows list the CMIP5 models, their resolution, global annual TC detections, for the late twentieth and twenty-first century, percentage change in TC detections, and a brief description of the models and data used in this study. The models are listed in order of resolution, with bold lines separating the high-, medium- and low-resolution models. Models with detections within ± 50% of that observed, highlighted in bold text, are used in the current analysis. (Reproduced from Table 2 of Tory et al. 2014.)

Table 3 The twelve CMIP5 models used in the study listed in grid resolution order (highest to lowest)

Model	Model code	lon × lat	$\xi(\times10^{-5}s^{-1})$	RH_{700} (%)	$V_{PI}(ms^{-1})$	$V_{sh}(ms^{-1})$	Family
bcc-csm1-1-m	**BCM**	320 × 160	2.0	40	40	20	BCC
CCSM4	CC4	288 × 192	2.0	**35**	40	20	–
CNRM-CM5	CN5	256 × 128	2.0	**30**	40	20	–
MIROC5	MI5	256 × 128	2.0	**35**	40	**22.5**	–
ACCESS1-0	**AC0**	192 × 144	**1.5**	**35**	40	**22.5**	ACC
ACCESS1-3	AC3						ACC
HadGEM2-ES	HG2						ACC
CSIRO-Mk3-6–0	CSI	192 × 96	**1.5**	*45*	**30**	20	–
GFDL-CM3	**GF3**	144 × 90	**1.5**	40	40	**22.5**	GFDL
GFDL-ESM2G	GFG	144 × 90	**1.5**	40	*45*	20	GFDL
GFDL-ESM2M	GFM						GFDL
bcc-csm1-1	**BC1**	128 × 64	**1.5**	40	40	20	BCC

The model names and model codes of the four representative models are in bold text. The default thresholds (same as those used in the development of the formation boundary concept in ERA-Interim data) are in plain text, with less restrictive thresholds in bold and more restrictive thresholds italicized. Model families are listed in the last column
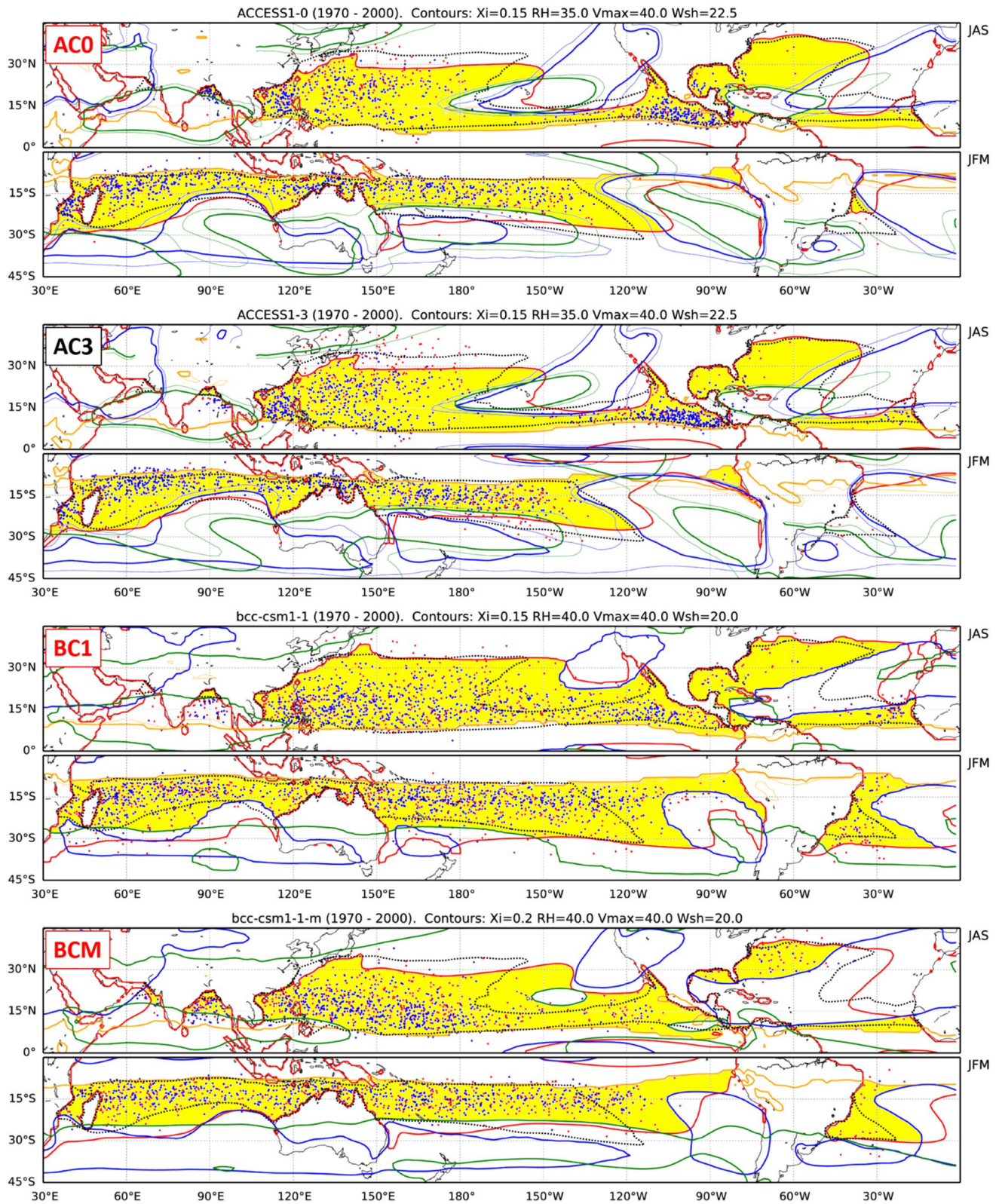
Fig. 2 As in Fig. 1 but for the CMIP5 models, historical scenario, with ERA-Interim boundaries (black dotted lines) included for comparison. Where retuned thresholds are used, original thresholds are included (fine contours) for comparison. Individual figure panels are labelled with the respective model abbreviations (Table 2). The representative four models (Sect. 2.4) have the model abbreviations in red text
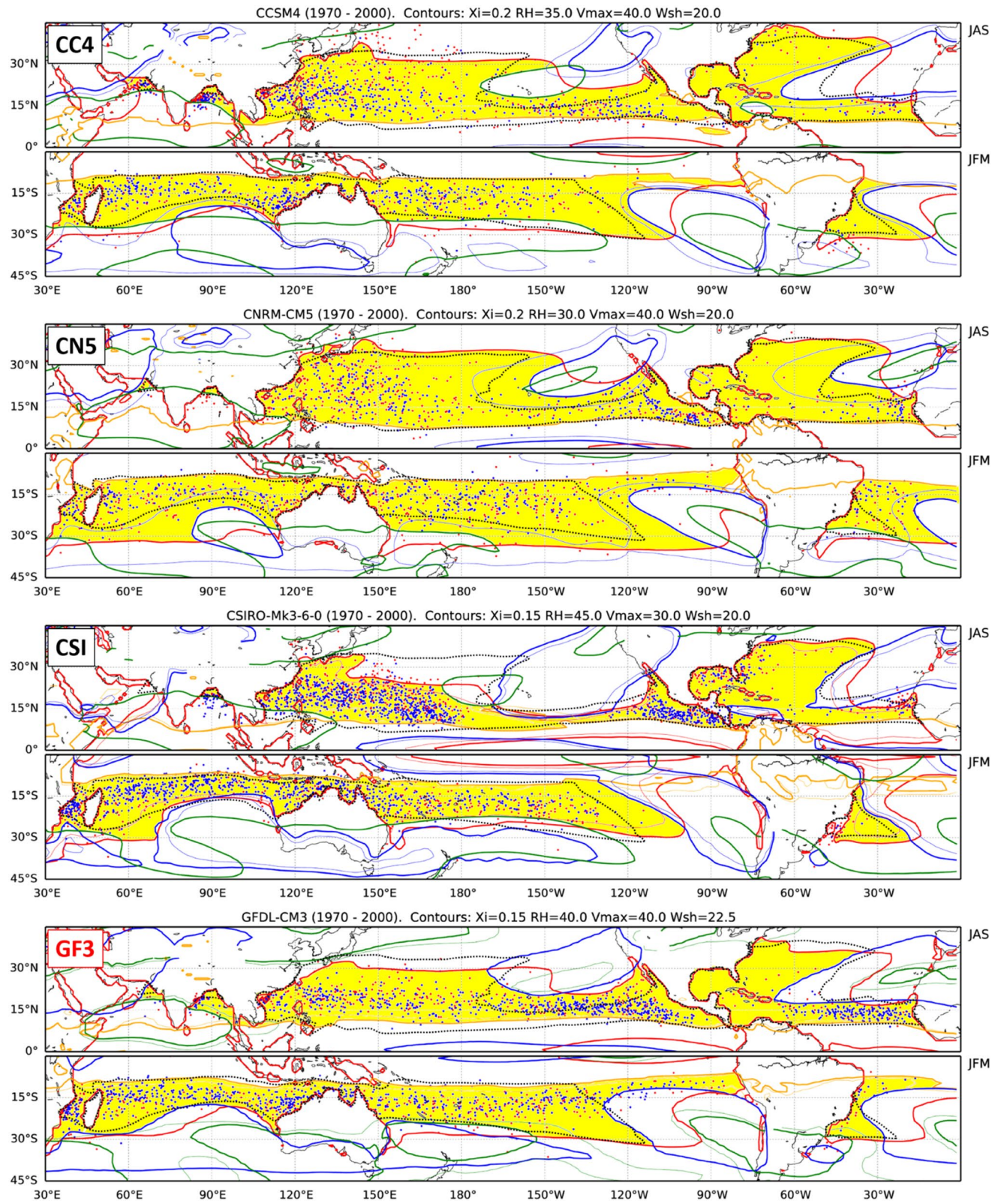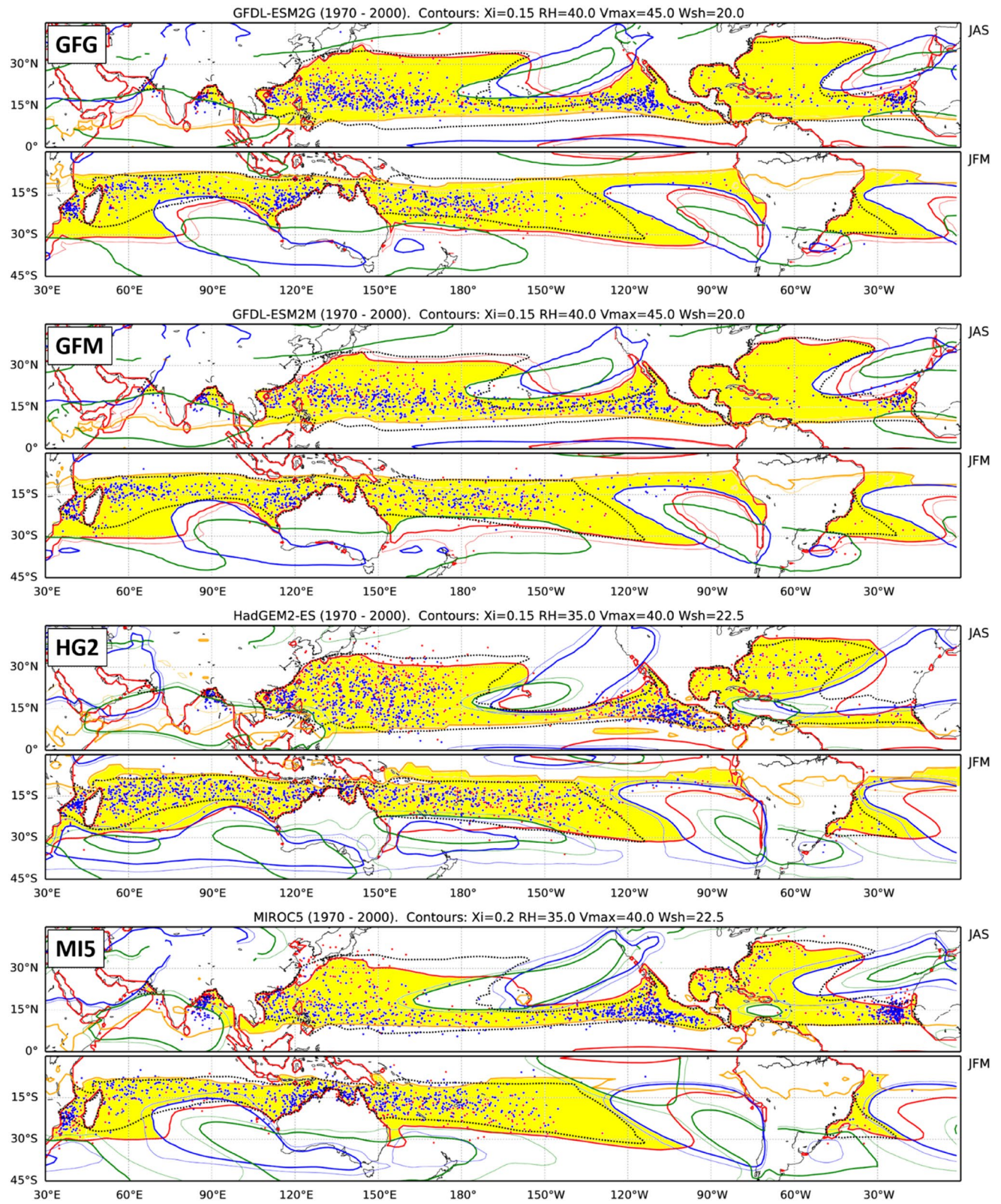
Fig. 2 (continued)

Fig. 2 (continued)

Geophysical Fluid Dynamics Laboratory, and the ACC family includes the two Australian Community Climate Earth-System Simulator (ACCESS) models plus version 2 of the Hadley Centre Global Environment Model (HadGEM2).

In the next two sections TC formation boundary plots are introduced for all twelve models, for the historical (Fig. 2) and rcp85 (Fig. 3) scenarios, with 31 seasons of TD and TS detection locations marked by red and blue dots, respectively. Total numbers of TD and TS detections for each model, scenario and basin are listed in Table 4 for the three summer months, January—March (southern hemisphere) and July—September (northern hemisphere). It is beyond the scope of this paper to analyse these detection distributions and changes; however the reader is referred to the series of papers that analyse the OWZP detected TS tracks, by Sam Bell and co-authors (Bell et al. 2018, 2019a, b, c, 2020a, b). To avoid unwieldy referencing within the text, model plots are referred to only by the model abbreviation (Table 3), and for easy reference, appear in alphabetical order in the figures.

3 CMIP5 model performance

All four of the selected models show the NI basin is made unfavourable by strong shear (Fig. 2), and in the remaining basins the basic pattern of broader favourable formation zones in the west than the east is evident (cf. Fig. 1). In general, the same threshold quantity patterns that determine the poleward and equatorward boundaries identified in the reanalyses are seen in these CMIP5 models. However, the favourable formation regions in each basin can vary substantially in geographic coverage between models and reality, with the most notable example the NA basin. Figure 2 shows that after the additional threshold fine-tuning (mentioned in Sect. 2.3) the threshold set (defining the favourable formation regions) do represent well the regions in which TCs are detected (red and blue dots) in each model, which provides some confidence that the relationship between large-scale global circulations and TC formation is reasonably well represented in the CMIP5 models by the four threshold quantities identified in ERA-Interim reanalysis data. A more detailed analysis follows for each ocean basin separately, culminating in a subjective performance assessment summarised in Table 5.

3.1 North Indian Ocean basin

The mid-summer analysis covers the period when the NI basin is dominated by the monsoon circulation, which brings very strong shear and strong cross-equatorial flow that pushes the ξ boundary far from the equator (as far as 15° north in the Arabian Sea, Fig. 1). Consequently, only

the northern-most parts of the Arabian Sea and Bay of Bengal see TC formation during these months. The active TC formation periods in the NI basin are limited to the shoulder seasons, when the oppressive monsoon influence is weaker. However, these transition seasons are difficult to analyse, due to the higher climatic variability, consequently projections for this basin are not made. However, it is still useful to investigate how well the models reproduce this "null" season.

Assuming Fig. 1 represents reality, a subjective comparison with the four representative models in Fig. 2 provides a qualitative performance assessment. The boundaries and detections are perhaps best captured by AC0. In BCM and GF3 the shear is a little weak providing a broader region of favourable conditions, which in the former appears to be responsible for unrealistically high numbers of TC detections. Interestingly, BC1 shows all the detections occurred inside the high shear region. This may indicate more shear variability in this model (TCs forming during reduced shear periods), or simply that TC-like circulations are less sensitive to shear in coarse resolution models.

A similar diversity in results is present in the remaining models. Of note is a reduced eastward extension of the shear threshold in CC4, GF3 and MI5, which opens up more of the Bay of Bengal for TC formation.

3.2 Western North Pacific Ocean basin

The poleward extent of this basin is determined by the V_{PI} threshold in ERA-Interim (Fig. 1) and in all twelve models investigated (Fig. 2). The V_{PI} boundary in BC1 is similar in latitude to the 35° diagnosed in ERA-Interim, while in the other three representative models it is located near 30° north. Perhaps as a consequence, TC detections in BCM and GF3 are concentrated south of about 25°, although TC detections in AC0 are less confined by this boundary. An equatorward bias of the V_{PI} threshold position is common to most models, with CSI the most extreme case. CN5 is an exception because it has excessive V_{PI} in most basins.

The equatorward boundary, determined by the ξ threshold is reasonably well represented in all four representative models, with the latitudinal variation west of 150° longitude best represented by AC0. Here the boundary in BC1 and BCM is formed instead by an eastward extension of the NI monsoon shear threshold (a pattern in CSI and HG2 also). The ξ threshold also defines well the equatorward boundary of the TC detections. Consequently, a poleward bias of the ξ threshold in GF3, together with the above-mentioned equatorward bias of the V_{PI} threshold, results in an overly narrow latitude band of TC formation in GF3.

The division between the West and East North Pacific basins is somewhat arbitrary. A logical boundary is where the latitudinally broad favourable formation region that
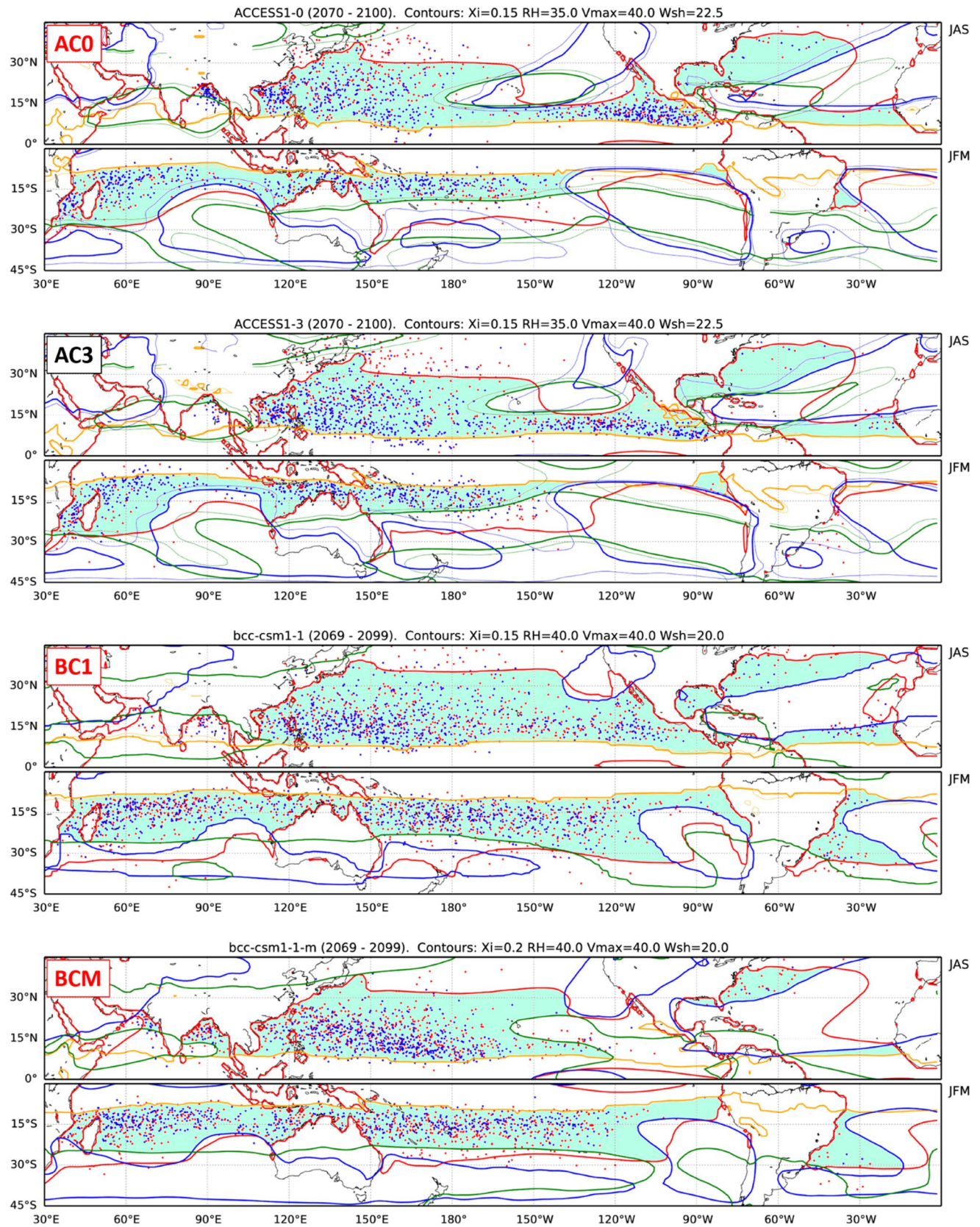
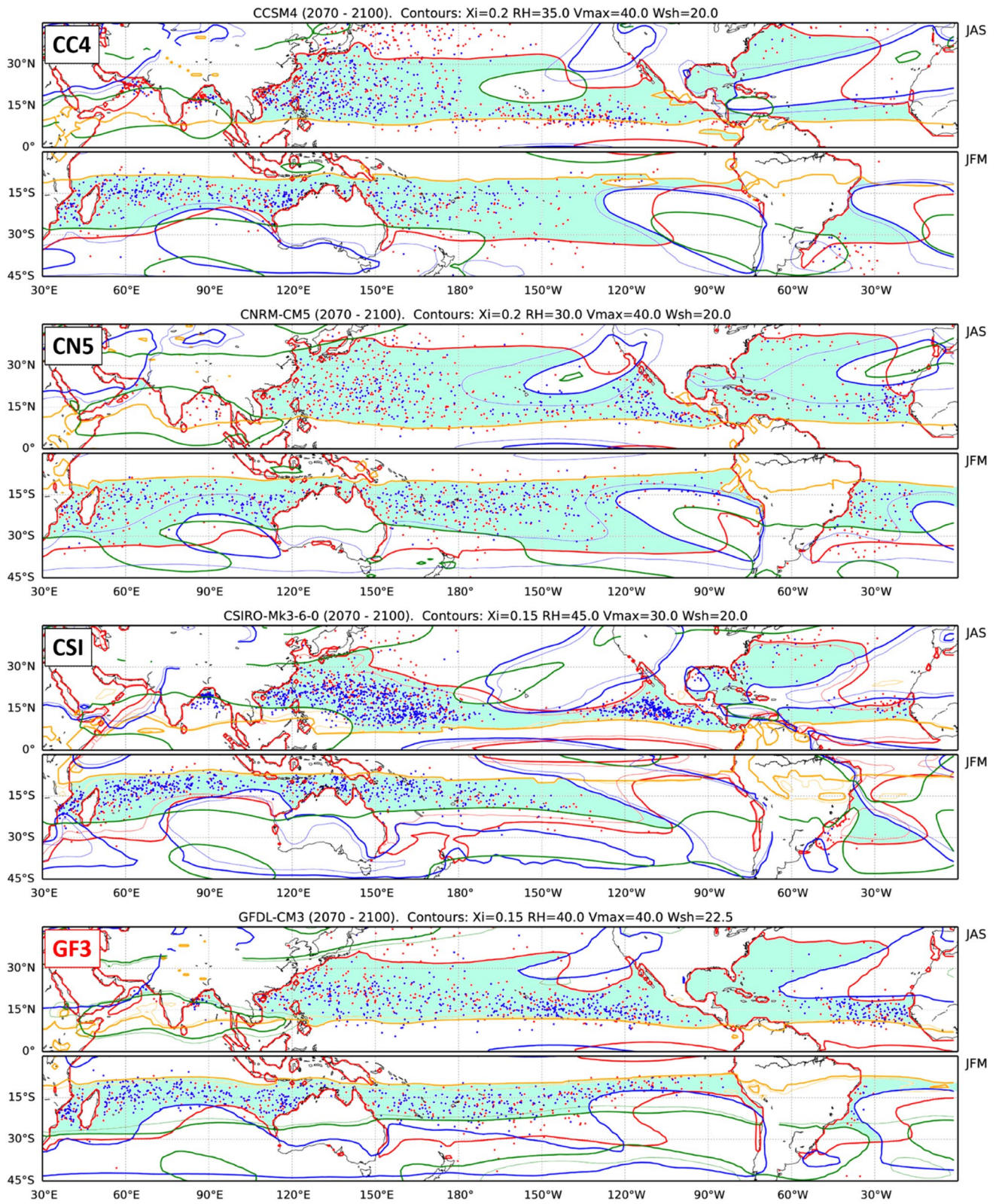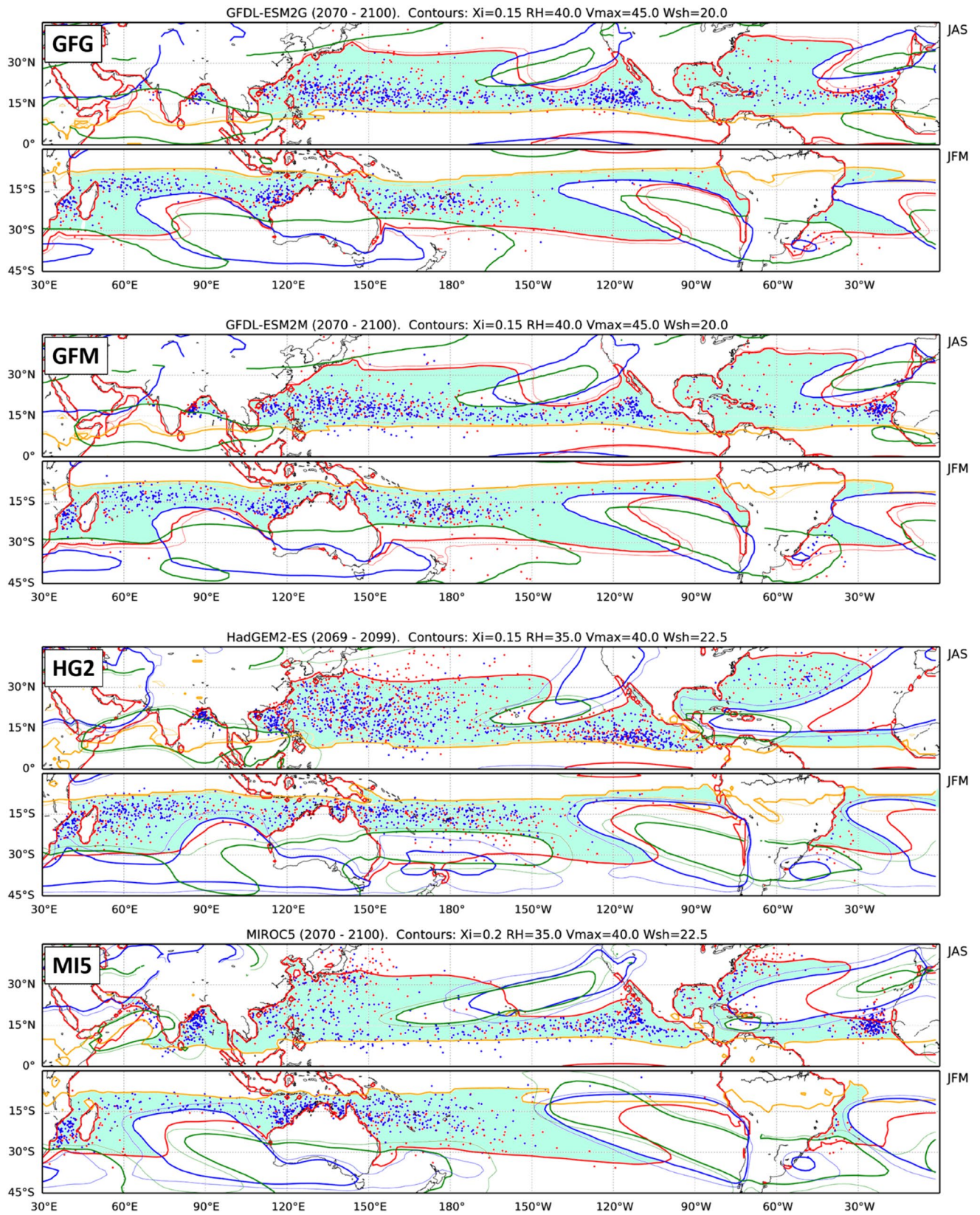**Fig. 3** As in Fig. 2 but for the rcp85 scenario

Fig. 3 (continued)

Fig. 3 (continued)

Table 4 Total number of Tropical cyclone detections for each basin for the summer months (July—September, northern hemisphere, and January—March, southern hemisphere)

	WNP	ENP	NA	SI	WSP	Aus	ESP	SA
ERA-Interim (1980—2010)	191/476	115/265	109/201	87/331	114/218	70/214	0/0	2/1
ACCESS1-0 (**AC0**)	**214/324**	**86/199**	43/48	**141/424**	**142/269**	**81/224**	**1/0**	5/0
	251/370	**112/248**	31/20	**112/244**	**100/202**	**46/122**	**0/0**	4/1
ACCESS1-3 (**AC3**)	**221/434**	**77/275**	52/48	**100/443**	**155/303**	**61/234**	**1/1**	8/0
	258/564	**106/246**	25/15	**90/276**	**82/237**	**35/158**	**4/2**	13/1
Bcc-csm1-1 (**BC1**)	**303/481**	143/208	71/42	**239/301**	300/429	**139/128**	41/32	55/27
	316/487	157/153	61/40	**273/281**	343/392	**132/112**	32/13	40/17
Bcc-csm1-1 m (**BCM**)	288/458	65/36	53/18	**190/258**	253/275	**107/154**	15/9	24/4
	383/499	60/32	29/6	**235/284**	369/293	**143/142**	11/4	15/6
CCSM4 (**CC4**)	**232/305**	**97/116**	47/36	**113/265**	**124/159**	**78/153**	4/1	**17/9**
	328/356	**134/108**	32/17	**135/263**	**126/135**	**85/147**	5/2	**24/11**
CNRM-CM5 (**CN5**)	**263/193**	77/146	64/56	150/163	195/184	102/89	17/13	45/40
	285/154	88/128	88/72	153/161	185/202	81/101	17/19	64/36
CSIRO-Mk3.6.0 (**CSI**)	293/643	67/230	138/99	**163/511**	170/245	103/276	**1/1**	**25/5**
	249/679	56/275	88/60	**95/341**	71/212	29/195	**2/0**	**18/6**
GFDL-CM3 (**GF3**)	172/236	111/315	50/173	**120/375**	139/234	64/203	15/26	16/17
	185/212	99/245	67/122	**92/316**	133/192	54/143	30/21	12/9
GFDL-ESM2G (**GFG**)	**155/464**	57/269	73/110	**86/363**	132/234	58/206	6/8	**6/4**
	163/400	65/263	83/161	**109/293**	127/173	91/188	8/8	**13/11**
GFDL-ESM2M (**GFM**)	**151/411**	68/222	51/70	**80/359**	111/242	48/186	4/18	**14/3**
	154/400	53/208	91/132	**78/319**	115/197	53/184	10/8	**9/16**
HadGEM2-ES (**HG2**)	**334/554**	**162/315**	93/82	**194/556**	246/362	121/295	14/11	20/15
	369/568	**199/293**	66/61	**150/367**	170/283	95/182	6/6	20/8
MIROC5 (**MI5**)	160/326	**73/368**	164/231	**112/389**	129/333	77/343	**0/1**	**10/9**
	178/252	**94/259**	156/197	**101/320**	109/245	91/291	**3/1**	**20/6**

Numbers of Tropical Depressions that did not become Tropical Storms and numbers of Tropical Cyclones that exceed Tropical Storm intensity (TD/TS) for historical (upper) and rcp85 (lower) scenarios. Equivalent numbers of TD/TS detections in ERA-Interim for the 31 summer seasons from 1980 to 2010 are included for comparison. See Fig. 1b for the basin domains and Table 1 for basin acronyms. Detection numbers from basins used in the projection analysis are shown in bold text

characterizes the WNP meets the characteristic latitudinally narrow eastern region. However, since the models differ substantially in how they represent the two basins and some produce a nearly uniform latitudinal width across the Pacific of the favourable formation region, it is necessary to comment specifically on model performance in the central Pacific where this boundary should be defined. In reality, favourable TC formation in the central Pacific is confined to a narrow latitude band between about 10 and 15° N, due to dry air and shear (Fig. 1) associated with the Tropical Upper Tropospheric Trough (TUTT, e.g. T18, Wang and Wu 2018). The TUTT is dynamically linked to the lower troposphere Pacific anticyclone through upper tropospheric convergence of the associated secondary circulation. All four representative models reproduce the TUTT-associated eastern Pacific dry air and shear, but with varying success (Fig. 2). AC0 best reproduces the pattern, correctly excluding the Hawaiian Islands, but with slightly too strong shear. BC1, BCM and GF3 fail to extend the dry air sufficiently into the central Pacific, and consequently there are too many TC detections there. CC4 is also too moist in the central Pacific, although

shear excludes TC formation near the Hawaiian Islands. In contrast dry air and shear extend too far into the central Pacific in CSI and MI5.

Interestingly, Wang and Wu's (2018) assessment of TUTT reproduction (using 200 hPa zonal wind, U_{200}, skill score) in 43 models also found MI5 performed relatively poorly, but another MIROC model (MIROC-ESM) had the worst skill score of all due to a westward bias of the TUTT location (see their Fig. 4). In contrast they found an eastward TUTT bias in GF3, which may explain the weak influence of dry air and shear in the GF3 central Pacific. They found AC0 and AC1, the models that best represent our central Pacific formation boundaries, had the best U_{200} skill scores.

Model performance in this basin is mostly judged on (1) the latitude of the northern boundary (too low [L], good [G], too high [H], compared with ERA-Interim), and (2) how well the TUTT and related circulations define the shape and position of the eastern boundary (too far west or too strong [Wstr], good [G], or too far east or too weak [Ewk]). The letter codes are listed in Table 5, along with an overall subjective performance assessment of Good, Pass or Fail.

Table 5 Summary of model errors for each basin

	WNP 2G 6P 4F	ENP 2G 5P 5F	NA 0G 0P 12F	SI 3G 8P 1F	WSP 1G 8P 3F	Aus 5G 6P 1F	ESP 3G 1P 8F	SA 1G 4P 7F	Number of basins used in projections per model
ACCESS1-0 (**AC0**) 2G 4P 2F	**L, G** Pass	**N, G** Pass	U, U Fail	**G, G** Good	**N, G** Pass	**G, N** Pass	**G, G** Good	G, N Fail	6
ACCESS1-3 (**AC3**) 1G 5P 2F	**L, G** Pass	**N, G** Pass	U, U Fail	**G, G** Good	**N, G** Pass	**G, N** Pass	**G, F** Pass	G, N Fail	6
Bcc-csm1-1 (**BC1**) 0G 3P 5F	**G, E** Pass	B, N Fail	U, U Fail	**B, G** Pass	B, E Fail	**G, B** Pass	B, M Fail	L, L Fail	3
Bcc-csm1-1 m (**BCM**) 0G 2P 6F	L, E Fail	B, N Fail	U, U Fail	**G, B** Pass	G, E Fail	**B, G** Pass	B, F Fail	S, L Fail	2
CCSM4 (**CC4**) 0G 6P 2F	**G, E** Pass	**B, G** Pass	U, U Fail	**B, B** Pass	**G, M** Pass	**B, G** Pass	N, F Fail	**G, L** Pass	6
CNRM-CM5 (**CN5**) 0G 1P 7F	**G, E** Pass	B, N Fail	U, U Fail	B, B Fail	B, M Fail	B, B Fail	B, M Fail	L, L Fail	1
CSIRO-Mk3.6.0 (**CSI**) 3G 2P 3F	L, W Fail	N, E Fail	U, G Fail	**B, G** Pass	**G, M** Pass	**G, G** Good	**G, G** Good	**G, G** Good	5
GFDL-CM3 (**GF3**) 3G 0P 5F	L, E Fail	B, N Fail	U, U Fail	**G, G** Good	**G, G** Good	**G, G** Good	B, M Fail	L, G Fail	3
GFDL-ESM2G (**GFG**) 3G 3P 2F	**G, G** Good	**G, G** Good	U, U Fail	**B, G** Pass	**G, M** Pass	**G, G** Good	B, F Fail	**S, L** Pass	6
GFDL-ESM2M (**GFM**) 3G 3P 2F	**G, G** Good	**G, G** Good	U, U Fail	**B, G** Pass	**G, M** Pass	**G, G** Good	B, M Fail	**S, L** Pass	6
HadGEM2-ES (**HG2**) 1G 4P 3F	**L, G** Pass	**N, G** Pass	U, G Fail	**B, G** Pass	**G, M** Pass	**G, G** Good	N, M Fail	L, G Fail	5
MIROC5 (**MI5**) 1G 5P 2F	L, W Fail	**G, E** Pass	U, G Fail	**B, G** Pass	**B, G** Pass	**G, B** Pass	**G, G** Good	**S, G** Pass	6
Number of models used in projections per basin	8	7	0	11	9	11	4	5	

The letter 'G' is used to indicate good performance, while other letters are used to indicate the performance limitations documented in Table 6. Two common limitations are identified for each basin, and the model performance judged on the extent of the limitations. Model performance summaries are provided in the first column below the model name, listing the number of basins ranked Good (G), Pass (P) or Fail (F). Similar summaries of how well each basin is represented are indicated in the first row. The last column lists the number of basins used in the projections per model, and the last row lists the number of models used in the projections per basin. The basins from each model used in the projection analysis are shown in bold text

The letter codes are described in Table 6. Only models listed Good or Pass are used in the projection assessment in Sect. 4.

3.3 Eastern North Pacific Ocean basin

Compared with the WNP the favourable TC formation region of the ENP basin is latitudinally narrow (Fig. 1). The equatorward boundary follows an almost constant latitude near 10° N, varying by only a few degrees, with the maximum poleward extent of about 12° N near 110° W. This is near the broadest part of the basin due to the poleward extension of the V_{PI} threshold towards the Baja Peninsula. Further west the V_{PI} threshold contracts equatorward where it meets the RH_{700} threshold, together confining the poleward extent of the formation region to 15° N as it extends into the central Pacific, where the TUTT influence dominates.

The ξ threshold is well represented in AC0 and GF3, but too close to the equator in BC1 and BCM (Fig. 2). The equatorward contraction of the V_{PI} threshold with distance west of 110° W is a little too large in AC0 and underrepresented in GF3, resulting in narrower and broader bands of favourable formation and corresponding TC detections, respectively. In both BC1 and BCM the V_{PI} threshold is too poleward, likely due to a weak Pacific anticyclone, with corresponding TC detections present at comparatively high latitudes (cf. Fig. 1). A concern for BC1 and BCM is too few detections east of 110° W, where TC formation density in the real world is very high. In these models, precursor disturbances propagating into the ENP from the North Atlantic are likely to be negatively impacted by very dry air and strong shear, especially in BCM (Fig. 2). Additionally, Sheffield et al. (2013) show the storm tracks in BC1 have a strong equatorward bias (near 8° N, see their Fig. 4), where in the real world TCs do
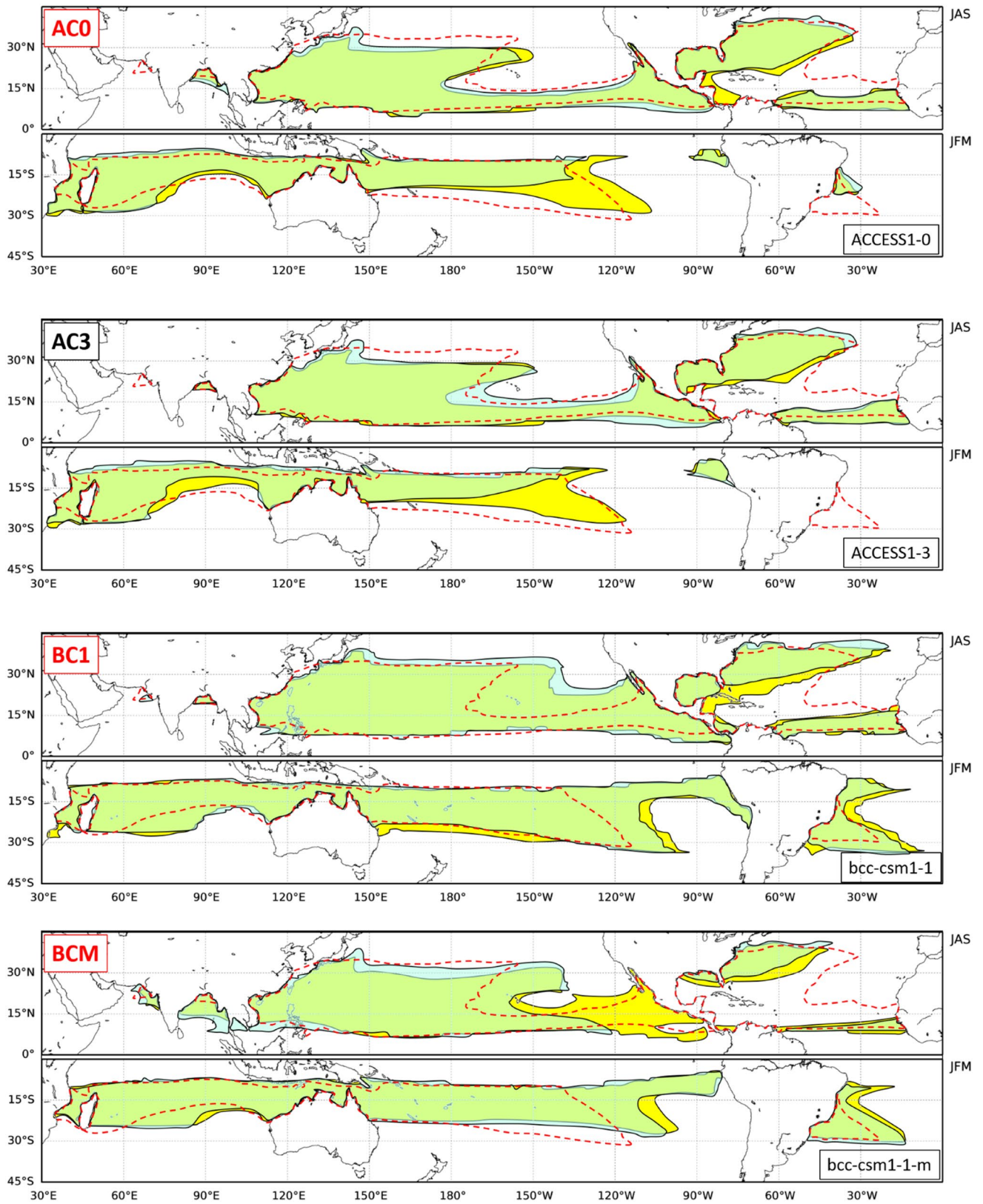
Fig. 4 Historical (yellow) and RCP85 (blue) TC formation boundaries overlayed. Overlapping boundaries appear green. The ERA-Interim boundaries from Fig. 1 (red dashed lines) are included for comparison
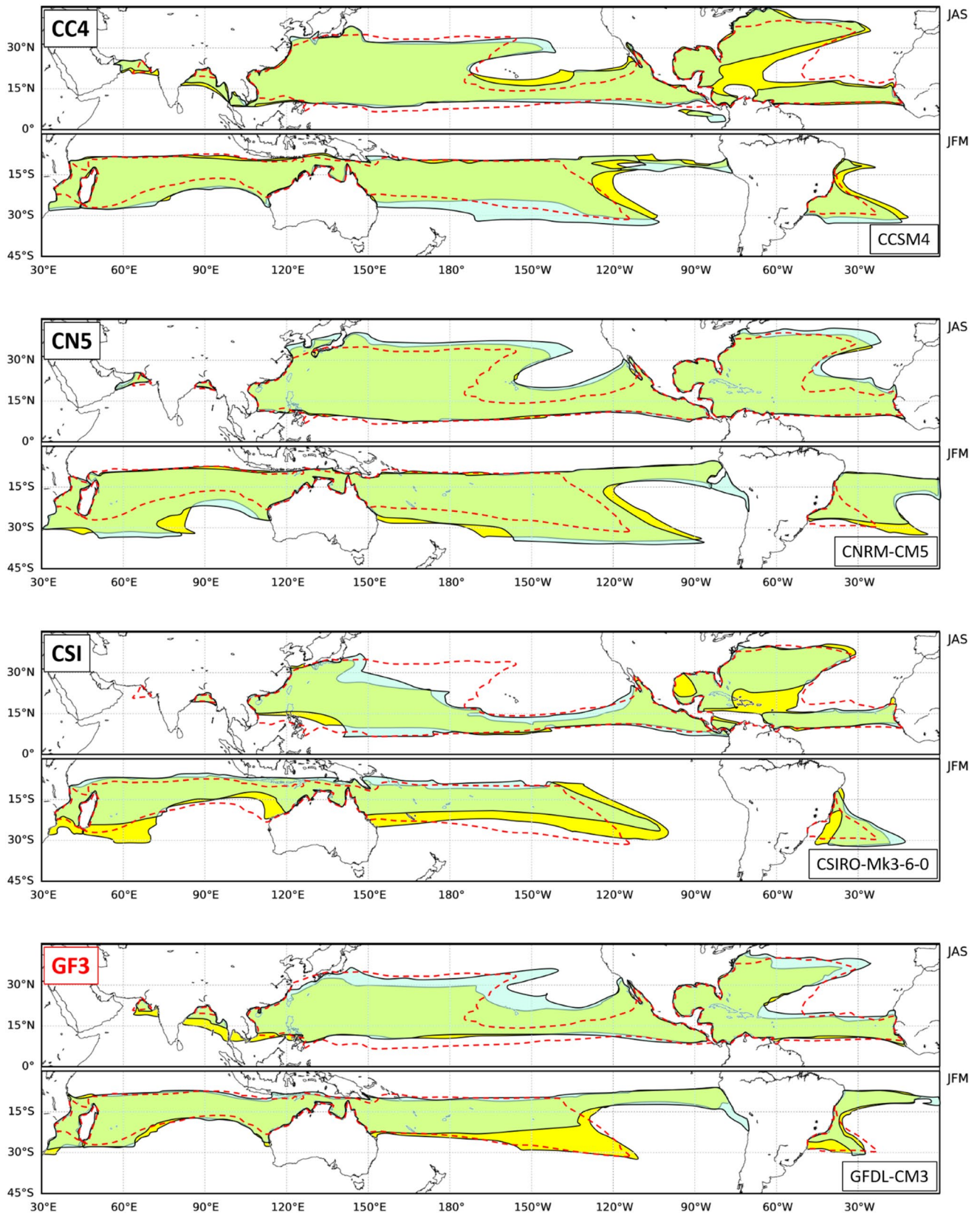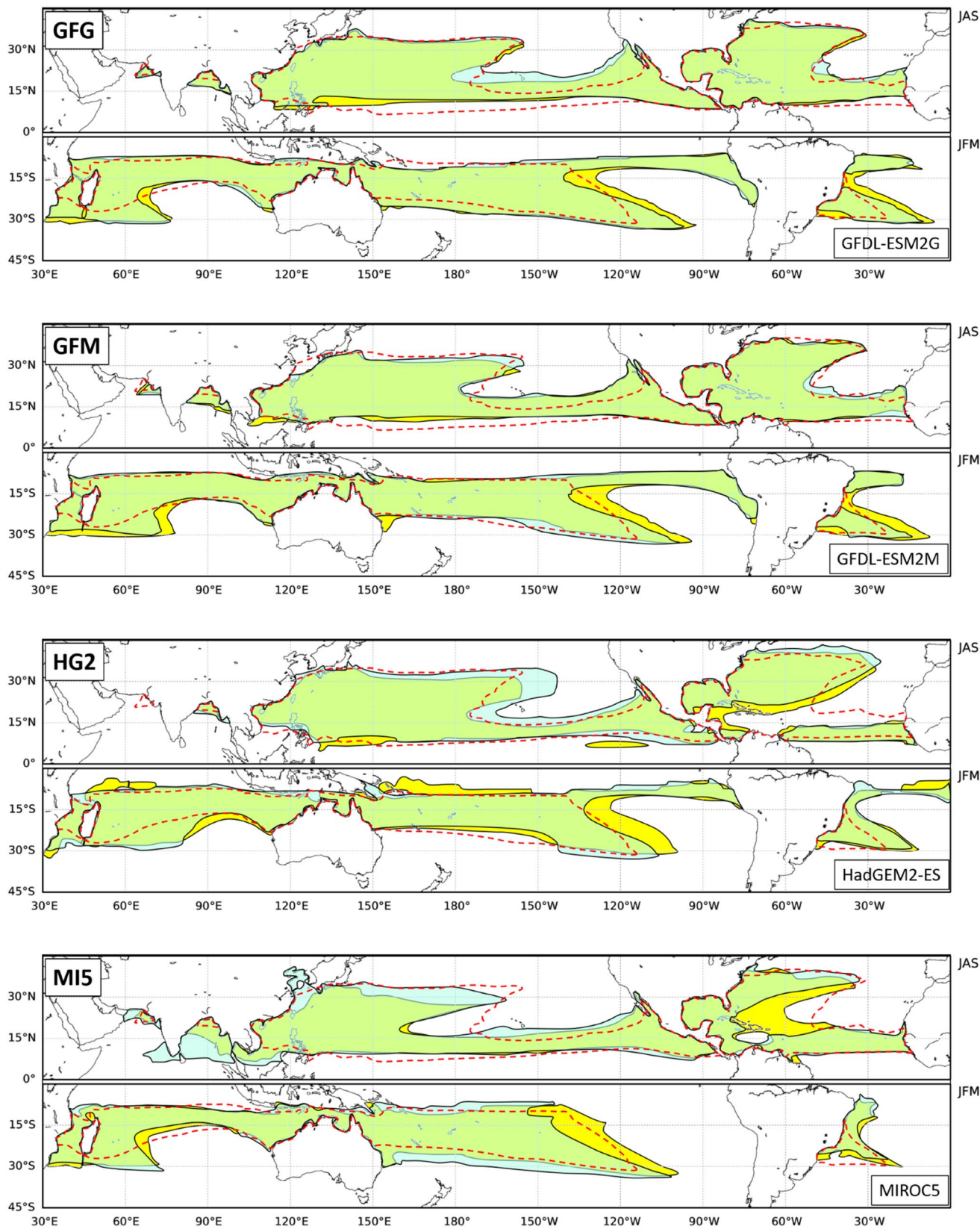
Fig. 4 (continued)

Fig. 4 (continued)

Table 6 Description of the two performance limitations for each basin, and their corresponding letter codes listed in Table 5

Basin	Basin-specific performance limitations
WNP	1—Latitude of the poleward boundary ('L' too low, 'H' too high)
	2—Position of the eastern boundary ('W' too far west, 'E' too far east)
ENP	1—North–south formation-band width ('N' too narrow, 'B' too broad)
	2—Exclusion of the Hawaiian Islands ('N' none, 'E' excessive)
NA	1—Formation zones and detections in latitudes < 25° N ('U' unsatisfactory, 'G' satisfactory)
	2—Formation zones and detections in higher latitudes ('U' unsatisfactory, 'G' satisfactory)
SI	1—North–south formation-band width in western half of the basin ('N' narrow, 'B' broad)
	2—North–south formation-band width in eastern half of the basin ('N' narrow, 'B' broad)
WSP	1—North–south formation-band width ('N' narrow, 'B' broad)
	2—Eastward bias of the eastern edge of the formation band (poleward of 15° S) ('M' moderate, 'E' excessive)
Aus	1—North–south formation-band width of eastern SI ('N' narrow, 'B' broad)
	2—North–south formation-band width of western WSP ('N' narrow, 'B' broad)
ESP	1—Presence of a southern ITCZ formation band ('G' not present, 'N' narrow, 'B' broad)
	2—Presence of TC detections ('G' none, 'F' few, 'M' many)
SA	1—Tropical formation band ('S' small and/or with few TC detections, 'L' large and/or with many detections)
	2—Higher latitude formation band ('N' none present, 'L' too large and/or too many TC detections)

not form. Their figure also shows a similar southward storm track bias for CC4, which also suffers from minimal TC detections west of 110° W and has the ξ threshold too close to the equator (Fig. 2).

The relationship between Sheffield et al.'s storm track bias and OWZP TC detections can be investigated in four additional models (CN5, GFM, HG2, MI5). HG2 and MI5 have small storm-track biases and healthy ENP TC detections. CN5 and GFM have slightly larger storm-track biases and fewer TC detections. Biases in storm track intensity identified by Sheffield et al. (2013) do not appear to be correlated with detection numbers except perhaps in the NA basin, where large-magnitude weak biases coincide with very few TC detections.

The performance in this basin is based on (1) the latitudinal width of the formation band (too narrow [N], good [G], too broad [B]), (2) the exclusion of the Hawaiian Islands (no [N], good [G], excessive [E]).

3.4 North Atlantic Ocean basin

In the eastern part of the NA basin favourable formation is confined south of 20° N by the V_{PI} and RH_{700} boundaries. Across the entire basin the ξ boundary is located at a near-constant 10° N (Fig. 1). The western half of the basin extends well north of 30° N, the most poleward of any ocean basin. The border between the narrow east and broad west is determined by the RH_{700} boundary, i.e., how far the dry air extends into the central NA basin. TC detections are relatively evenly dispersed apart from higher concentrations off

the African coast and slightly higher concentrations towards the western regions.

This basin is poorly modelled by all 12 CMIP5 models. With respect to TC detections, four models (AC0, AC3, BCM, HG2) produce very few TCs at lower latitudes (equatorward of 15° N), and nearly all models produce very few TCs, or none at all, in the Gulf of Mexico and the north west of the basin (Fig. 2).

Dry air extends too far westward in all of the four representative models. While it is a minor flaw in GF3, it is excessive in BC1 and BCM, leading to gaping TC formation holes that split the basin into two parts: southeast and northwest (Fig. 2). A similar TC formation hole is present in AC0 due to a combination of large westward dry air extension and excessive shear. Similar basin splitting (TC formation holes)[3] are also evident in AC3 and HG2, and to a lesser extent in CC4, CSI and MI5 (Fig. 2).

Considering the two parts of the split basin separately, Fig. 2 shows GF3 produces an abundance of TCs in the southeast part, BC1 produces a small number, and AC0 and BCM very few. The ability of models to produce TCs in these regions may be related to how broad in latitude the favourable formation band is and its proximity to the equator. For example, the favourable TC formation band in GF3 extends between about 10 and 18° N, closely matching the

---

[3] The TC formation hole is also evident in Fig. 5 of Sheffield et al. (2013) for three models in common with our study (GFM, HG2, MI5), in which a fundamentally different TC detection algorithm was used (Camargo and Zebiak 2002).

observed band (Fig. 1), whereas AC0 spans 8–13° N, which is both narrower and more equatorward than observed. We speculate that if the favourable region is too narrow and positioned too far equatorward, the propagation of African Easterly Waves (AEWs, known to be the dominant TC precursor in this region) will not align with the favourable TC formation region.[4] AC3 and HG2 also have too narrow and too equatorward southeast formation regions with very few TC detections. Conversely, studies in regional climate models that suppressed AEWs found TCs formed in similar numbers, but within other disturbances (Patricola et al. 2018).

AEW limitations in CMIP5 models have been documented by Dixon et al. (2017, too few AEWs because the Saharan Heat Low is too far westward) and Martin and Thorncroft (2015), insufficient convective diabatic AEW enhancement over poorly resolved Guinea Highlands), but the results are generalised, and thus unable to be related to individual model performance.

To the north and west of the split basin few TC detections appear in AC0, BC1 and GF3, despite the diagnosed favourable formation environment (Fig. 2). We speculate that very few precursor storms with the potential for TC formation make it to this side of the basin, due to a combination of too few precursor disturbances entering the NA basin in the east, and an environment too hostile to support amplification or precursor development in the central NA basin. Other models that show a low detection bias in the northwest include: AC3, CC4, GFG and GFM. All twelve models fail to produce reasonable TC climatologies in at least one of the southeast, Caribbean or northwest regions.

The failure of the models to produce TCs in the northwest region where the formation boundaries do suggest the formation environment is favourable, meant that good model performance had to also consider detection distributions. The basin is divided into two regions, lower latitudes (L, < 25° N, Africa to the Caribbean) and higher latitudes (H, > 25° N). Each region is rated either good (G) or unsatisfactory (U).

3.5 South Indian Ocean basin

The best performing basin in all models is the SI basin. Of the representative four, GF3 best captures the shape and relative locations of the threshold boundaries and has the best distribution of TC detections (cf. Fig. 1, 2). Compared with ERA-Interim, the equatorward boundary in GF3 is slightly poleward, and slightly equatorward in the other three models. AC0 also performs well, although the meridional

variation of the RH_{700} threshold across the basin is exaggerated, producing a poleward bias in the threshold position in the west. However, the bias is compensated for by the V_{PI} threshold taking over to define the formation boundary. Similar RH_{700} biases are present in BC1 and BCM, but the compensating threshold that defines the TC formation boundary in those models is V_{sh}. In fact, the RH_{700} bias is present in all 8 remaining models with V_{PI} compensating in AC3, CN5, CSI, GFG, GFM, HG2 and MI5, and V_{sh} compensating in CC4.

The relatively good performance of the models in this basin (only CN5 fails), allows a more critical performance assessment. The performance reported in Table 5 represents (1) the western and (2) eastern halves of the basin, based on the latitudinal width of the favourable formation region (narrow [N], good [G], broad [B]).

3.6 West South Pacific Ocean basin

West of 150° W, the TC formation boundaries are well-reproduced by all models except CN5. Of the four representative models, GF3 best reproduces the TC formation boundaries and distribution of TC detections. Like the SI basin AC0 is the next best performer, although strong shear and a slightly too poleward location of the ξ boundary combine to produce a latitudinally narrow TC formation region. The opposite is true for BC1, where all poleward thresholds are located too far south, broadening the TC formation region a few degrees too far poleward. BCM better reproduces the meridional width of the formation region, but it is too zonal, i.e., it fails to capture the slight poleward expansion of the South Pacific Convergence Zone towards the centre of the ocean basin. A too latitudinally-broad formation region is also present in BC1, CN5, GFG and MI5 due to the RH_{700} boundary being almost absent, and either or both the V_{PI} and V_{sh} boundaries located too far poleward. HG2 has the ξ boundary more equatorward than any other model between 150 and 180° East, due to low values of β^* there (Fig. 2). We assume it is an anomaly, since there are no TC detections and it is not present in the rcp85 climate (Fig. 3).

Like its northern counterpart the eastern boundary of the WNP can be defined by the eastward extent of the higher-latitude TC formation region. This boundary is also influenced by the TUTT and associated circulation, imposing shear and subsiding dry air on the region (c.f. Sect. 3.2). All models under-represent the TUTT and associated processes, leading to the eastern WSP boundary extending too far eastward. Consequently, model performance assessment in this basin is determined by (1) the latitudinal width (narrow [N], good [G], broad [B]) and (2) the location of the eastern-most edge poleward of 15° S (Good [G], moderately eastward [M], excessively eastward [E]).

---

[4] Only AEW disturbances that propagate through the easterly jet critical layer develop (e.g., Dunkerton et al. 2009; Asaadi et al. 2016, 2017).

3.7 Australian region

The Australian region makes up the east and west of the previous basins respectively, where the models perform best. Between the two basins the Australian continent defines the poleward boundary (110—155°E) and is thus fixed for all models. Equatorward the ξ boundary is reasonably well represented by each model, although in AC0, BC1 and BCM it extends slightly equatorward than that diagnosed in ERA-Interim (Fig. 1).

The performance summarised in Table 5 is determined by the latitudinal width of (1) the eastern SI and (2) the western WSP basins (narrow [N], good [G], broad [B]).

3.8 East South Pacific Ocean basin

This basin is the home of the infamous Pacific cold-tongue bias and double ITCZ, in which most climate models in the past, and many continue to, produce a southern hemisphere ITCZ (that mirrors the northern ITCZ) extending across the entire Pacific Ocean (e.g., Li and Xie 2014). The RH_{700} boundary in Fig. 1 shows that in reality, very dry conditions extend deep into the tropics suppressing convection in the eastern half of the South Pacific Ocean basin, which takes an enormous "bite" out of this tropical region within which TCs do not form. Even without the dry air, much of the basin (east of about 110° W) would be hostile to TC formation, due to overlapping V_{PI} (from the south) and ξ (from the north) boundaries and strong shear. The V_{PI} and ξ boundary overlap is due in part to a more poleward location of the ξ boundary (12—13°S) compared with almost all favourable TC formation regions (e.g., 7—10°S in most of the WNP, ENP, NA, SI and WSP basins). This is due to the absence of low-latitude convection in the ESP.[5]

In all 12 models investigated, all four threshold boundaries are less restrictive than reality (cf. Figs. 2 and 1). This is especially so for those models with a prominent southern ITCZ (including BC1, BCM, CN5, GF3, GFG and GFM, Fig. 2), which contributes to a more equatorward position of the ξ boundary (as mentioned above). Indeed, all models show the ξ boundary sloping equatorward from west to east across the Pacific (Fig. 2), rather than poleward (Fig. 1). The other three threshold boundaries contribute to a much-reduced eastern Pacific "bite" leaving behind in most models a narrow ITCZ-like band of favourable formation. CSI and MI5 do not produce an ITCZ-related favourable formation band, and AC0 and AC3 produce only small regions of favourability in the far east of the basin (Fig. 2).

The model performance in this basin is based on (1) the presence of a southern ITCZ-related favourable formation band (Not present [G], Narrow [N], broad [B]), and (2) whether detections are present (None present [G], few present [F], many present [M]).

3.9 South Atlantic Ocean basin

In the ERA-Interim reanalyses the SA basin is dominated by dry air that extends across the entire ocean from east to west, leaving only a small band of favourability off the Brazilian coast at relatively high latitudes. Very few TCs form here. Only two were detected by the OWZP scheme in ERA-Interim in a 34-year period. Many models fail to reproduce this extensive cross-ocean advection of dry air (defined by the RH_{700} boundary position), resulting in larger areas diagnosed to be favourable for TC formation, that contain TC detections. These include BC1, BCM, CN5, GF3 and to a lesser extent HG2 (Fig. 2). GFG and GFM also have larger favourable formation areas, but they contain relatively few detections.

Insufficient extension of dry air across the SA basin produces in some models two somewhat distinct formation regions, consisting of an enlarged higher latitude formation region off Brazil, and a tropical band that may extend part way or entirely across the ocean basin (e.g., GF3, Fig. 2). How far the tropical band extends across the basin is also determined by the position of the ξ boundary, with more equatorward positions further opening the space between the ξ and RH_{700} boundary. Models with a tropical band containing detections include BC1, BCM, CN5 and GF3, and to a lesser extent HG2 and MI5 (Fig. 2).

Performance in this basin is based on (1) the existence of the tropical formation band with detections (not present [G], small and/or contain few detections [S], large and/or contain many detections [L]) and (2) the presence of the higher-latitude band (not present [N], realistic size with few detections [G], large and/or contain many detections [L]).

3.10 Model performance summary

Table 5 summarises model performance and individual basin representation by the 12 models (last row). If two performance measures in a basin are rated 'G' then that basin is rated 'Good'. If only one performance measure is rated 'G', or none are rated 'G' the basin is usually rated 'Pass' and 'Fail' respectively (with eight and three exceptions respectively). These eleven exceptions result from a secondary subjective performance assessment that awards a Pass to two relatively minor biases, and a Fail when a single bias is severe. The worst performing basin is the NA, in which

---

[5] Low-latitude convection, such as the ITCZ, enhances lower troposphere absolute vorticity, which increases ξ (Eqs. 1 and 2) and contributes to a more equatorward position of the ξ boundary. See the discussion in Sect. 4 of T18.

Table 7 Projection summaries for the selected ocean basins

Basin	Number of models	Projection summary
WNP	8	Slight poleward expansion due to shift in V_{PI} boundary (AC0, AC3, BC1, CN5, CSI, GF3). Two models show minimal change (CC4, GFG)
ENP	7	Expansion in five models (AC0, AC3, GFG, HG2, MI5) with no change in GFM and a slight contraction in CC4
SI	11	Six models (AC0, AC3, BCM, CSI, HG2, MI5) show a contraction in the eastern basin due to an equatorward shift of the poleward boundary. Four models (CC4, GF3, GFG, GFM) show no change and BC1 shows a slight expansion
WSP	9	Five models (AC0, AC3, CSI, GF3, HG2) show a contraction due to an increase in windshear that shifts the poleward boundary equatorward, especially in the central Pacific. GFG shows no change, and GFM minimal expansion in the central Pacific. Two models (CC4, MI5) show expansion, the former due to reduced windshear, and the latter due to a poleward shift of the V_{PI} boundary
Aus	11	Four models (AC0, AC3, CSI, HG2) show a contraction to the east and west of Australia with three other models (BCM, MI5 GF3) showing a contraction in one of these regions. Two models (GFG, GFM) show no change in both the east and west. No model shows an expansion both to the east and west. (see SI and WSP entries)
ESP	4	Four models (AC0, AC3, CSI, MI5) show V_{PI}, RH_{700} and V_{sh} become more restrictive (consistent with an intensification of the atmospheric and oceanic anticyclone). The current highly unfavourable region will become more unfavourable in the future (i.e., zero TC formation will continue)
SA	5	Three models (GFG, GFM, MI5) show a slight contraction due to RH_{700} and V_{sh} boundaries becoming more restrictive. CSI shows a slight eastward expansion due to a RH_{700} boundary shift, and CC4 shows a slight poleward expansion due to a V_{PI} boundary shift. TCs will continue to be very rare events in the SA basin

Here the terms 'contraction' and 'expansion' refer to a north–south narrowing and broadening respectively of favourable formation regions

all 12 models failed the subjective performance assessment, hence it is excluded from the projection analysis. As noted previously the NI basin is also excluded. The ESP and SA basins performed poorly with 8 and 7 deemed failures respectively, suggesting projections made in these basins should be treated with a degree of caution. The remaining four basins plus the Australian region have more than half the models passing the performance assessment.

4 Future changes in TC formation regions

In this section limited projections are proposed for all TC basins except NI and NA. The projection assessment, summarised in Table 7, is subjective and based on changes in TC formation boundary locations between the historical (Fig. 2) and rcp85 (Fig. 3) scenarios. The historical and rcp85 boundaries are overlaid for easy comparison in Fig. 4.

4.1 Western North Pacific Ocean basin

All eight models included in the WNP projection analysis show a small poleward expansion of the poleward boundary (Fig. 4), due to a poleward shift of the V_{PI} boundary (Fig. 3). This change is accompanied by increased numbers of TC detections, which may signal a poleward expansion of TC formation in a future warmer climate. However, a general increase in TC detections that fall outside the boundary is

noted,[6] perhaps indicating that the TC detection methodology, or the TC boundary analysis, is not ideal at these high latitudes in the RCP85 climate.

The central North Pacific errors in the TC formation boundaries attributed to TUTT-circulation biases (Sect. 3.2) persist in the RCP85 climate for all models, with only small changes. Five of the eight WNP models show minimal change in the WNP eastern boundary position (AC0, CC4, CN5, GFG, GFGM), whereas AC3, BC1 and HG2 show a small *eastward* expansion (Fig. 4), which may be related to future changes in El Nino events (Bell et al. 2020a). This change is not likely to be associated with shifts in TUTT location, since both AC0 and HG2 experienced a 2° longitude *westward* shift of the TUTT location, according to Fig. 6d of Wang and Wu (2018).[7]

4.2 Eastern North Pacific Ocean basin

The ENP has seven models included in the projection analysis, six in common with the WNP (Table 5). AC0, shows a slight north–south expansion of the favourable formation zone (Fig. 4). A similar pattern is also present in AC3, GFG, HG2 and MI5, whereas GFM shows very minimal change.

---

[6] Only a small proportion are diagnosed as TSs (blue dots), indicating that while TC detections are increasing, the environment remains quite hostile to development beyond TD intensity.

[7] The only other model in common between the WNP eight and the Wang and Wu (2018) analysis, CN5 showed minimal change in the TUTT location and the WNP eastern boundary (Fig. 4).

In each case the poleward expansion extends towards the Hawaiian Islands, and even envelops the islands in GFG. Only CC4 shows the opposite behaviour with a contraction of the favourable formation zone away from the Hawaiian Islands (Fig. 4). An expansion of the TC favourability zone towards the Hawaiian Islands from the west is also evident in AC3, GFG and HG2 (Fig. 4), due to increased RH_{700} and reduced shear (cf. Figs. 2 and 3).

The consensus projection is for a slight latitudinal expansion of the TC favourability zone across most of the ENP, with TC formation becoming more favourable near the Hawaiian Islands, potentially from two directions, the south and west. This change may be associated with a common CMIP5 future of a more El Nino-like state in which the central Pacific warms more than the west (e.g., Chand et al. 2017, Bell et al. 2020a). Recently, Seager et al. (2019) questioned this warming scenario, suggesting it may be an artefact of the cold-tongue bias (Sect. 3.8) present in many CMIP5 models, in which case the western ENP might experience minimal TC formation boundary changes.

4.3 South Indian Ocean basin

The SI is the best performing basin, with only one model (CN5) failing the subjective performance assessment (Table 5). Changes in the position of the equatorward boundary are generally small, with most models showing no perceptible change, or a slight equatorward shift.

Six models (AC0, AC3, BCM, CSI, HG2 and MI5) show an equatorward shift of the poleward boundary in the east of the basin (near the Australian continent, generally due to decreasing RH_{700}, cf. Figs. 2 and 3) contributing to a meridional narrowing of the region of favourable formation. Exceptions include CC4, GF3, GFG and GFM, which show no shift, and BC1 shows a slight poleward shift of the boundary (Fig. 4).

The meridional narrowing in the east is consistent with changes in the Indian Ocean Dipole (IOD) suggested by Zheng et al. (2013). Their analysis showed an ensemble-mean strengthening of the SST gradient across the ocean basin (greater warming in the west than east), accompanied by a strengthening of the trade easterlies (weakening of the Walker Circulation) and a thinning of the thermocline in the east of the basin. Of the seven models in common with our study, the strongest changes in the IOD they identify match models with a well-defined contraction of the favourable formation zone (CSI, GFM and MI5). Additionally, Bell et al. (2020a) found a substantial reduction of TC detections in the eastern SI basin during future El Nino events.

These results suggest a plausible future scenario is for a weakening of the Walker Circulation, leading to a strengthening of the trade easterlies and SI basin anticyclone, which narrows the favourable formation zone in the east of the basin.

4.4 Western South Pacific Ocean basin

Only three models failed the WSP subjective performance test (BC1, BCM and CN5). Common to most models and basins the V_{PI} threshold moved slightly poleward in rcp85 (Fig. 3) compared with the historical scenario (Fig. 2), but this only produced an expansion in the formation region in MI5. In most models it was countered by an increase in windshear producing a contraction of the formation region (AC0, AC3, CSI, GF3 and HG2, Fig. 4) that is generally larger in the central South Pacific than nearer the Australian continent. The opposite change, a slight poleward expansion of the formation boundary, is found in CC4 and to a lesser extent GFM, due to decreasing windshear.

Again, changes to the equatorward boundary are minimal. Exceptions include an equatorward expansion in CSI and MI5. (We ignore the apparent contraction in HG2 associated with the suspected anomalous low-latitude favourable region between 150 and 180° East in Fig. 2, mentioned in Sect. 3.6).

A plausible future scenario for the WSP basin is for increasing wind shear to override and reverse any poleward expansion tendency associated with increasing V_{PI}.

4.5 Australian region

The Australian region incorporates the best performing parts of the SI and WSP basins. A combination of minimal change in the equatorward boundary with an equatorward shift of the poleward boundaries to the east and west of the Australian continent, suggest a contraction of the TC formation band is plausible in the Australian region.

4.6 Eastern South Pacific Ocean basin

Only four models (AC0, AC3, CSI and MI5) were deemed suitable for a projection analysis in ESP (Table 5). All four models show the three threshold quantities V_{PI}, RH_{700} and V_{sh} become more restrictive in the future scenario (Fig. 4). The small favourable formation zones in AC0 and AC3 in the ESP far east, noted in Sect. 3.8, show little change in the rcp85 future (Fig. 3). The four-model consensus of a more hostile future environment for TC formation, in a region that currently never experiences TCs, suggests the region will continue to be devoid of TCs.

4.7 South Atlantic Ocean basin

Five models passed the subjective performance assessment (CC4, CSI, GFG, GFM and MI5) for the SA basin (Table 5).

The RH_{700} and V_{sh} quantities tend to become more restrictive (c.f. Figs. 2 and 3), leading to a general contraction of the favourable TC formation region. Minor exceptions include, a slight eastward expansion in CSI due to a shift in RH_{700}, and a slight poleward expansion in CC4 due to a shift in V_{PI}.

All boundary changes in these models are minor, although most suggest a contraction of the favourable TC formation region. Thus, continued very infrequent TC formation is plausible.

5 Summary

Motivated by a desire to understand why TCs form where they do in climate models, T18 developed a set of threshold quantities that defined TC formation, using TC detections in ERA-Interim data. In this paper the thresholds and detections are applied to twelve CMIP5 models for the historical and rcp85 scenarios. Results from the application to the historical scenario were used to assess each model's ability to recreate realistic mid-summer-season TC formation climatologies. A subjective performance assessment for each TC basin in each model was used to determine which basin/model pair could be used in the projection analysis. This paper only provides a general assessment of model performance and projections, due to the large number of model/basin combinations.

A considerable variation in performance was found between models and between individual basins within models (Table 5). The NI basin was excluded from the projection analysis because few TCs form in the mid-summer study period, when monsoon shear suppresses formation. The NA basin was also excluded because all twelve models failed to reproduce realistic TC formation climatologies, mostly because the basin was too dry and the shear too strong. The Australian region was best represented with eleven of the twelve models passing the performance assessment, due largely to good performance in the neighbouring SI and WSP ocean basins. The ESP and SA basins were in general not well-reproduced with only four and five models passing respectively, whereas the northern Pacific basins were better represented with eight models included in WNP and seven in ENP. A common problem in the ESP was the presence of a southern hemisphere ITCZ enabling TC formation across the entire South Pacific. Confidence in projections was reflected in the number of models that passed the performance assessment for each basin.

Projections, expressed as plausible scenarios (summarised in Table 7), are based on consensus changes in formation boundary threshold locations and TC detection. Minimal change in the WNP basin boundaries is proposed, with perhaps a slight poleward expansion, but into a relatively hostile environment where a high proportion of TDs fail to become TCs. A slight meridional broadening is proposed for the ENP, with a possible extension towards the Hawaiian Islands. In the SI basin a contraction in the east due to an equatorward shift of the poleward boundary is proposed, likely due to a strengthening of the oceanic and atmospheric anticyclones. A similar contraction is proposed for the WSP, but due to increased wind shear instead, although the models that do not show increased shear suggest a slight poleward expansion is possible. The Australian region, bordered by these two basins, shares the same general projection of contracting favourable formation regions. While the ESP and SA basins are generally not well represented by the models, the consensus results suggest the already highly unfavourable TC formation environments will become even more unfavourable.

References

Asaadi A, Brunet G, Yau MK (2016) On the dynamics of the formation of the Kelvin Cat's-eye in tropical cyclogenesis. Part I: Climatological investigation. J Atmos Sci 73:2317–2338. https://doi.org/10.1175/JAS-D-15-0156.1

Asaadi A, Brunet G, Yau MK (2017) The importance of critical layer in differentiating developing from nondeveloping easterly waves. J Atmos Sci 74:409–417. https://doi.org/10.1175/JAS-D-16-0085.1

Bentsen M, Bethke I, Debernard JB, Iversen T, Kirkevåg A, Seland Ø, Drange H, Roelandt C, Seierstad IA, Hoose C, Kristjánsson JE (2012) The Norwegian earth system model, NorESM1-M. Part 1: description and basic evaluation. Geosci Model Dev Discuss 5:2843–2931

Bell SS, Chand SS, Tory KJ, Turville C (2018) Statistical assessment of the OWZ tropical cyclone tracking scheme in ERA-Interim. J Clim 31:2217–2232. https://doi.org/10.1175/JCLI-D-17-0548.1

Bell SS, Chand SS, Tory KJ, Dowdy AJ, Turville C, Ye H (2019a) Projections of Southern Hemisphere tropical cyclone track density using CMIP5 models. Climate Dyn 52:6065–6079. https://doi.org/10.1007/s00382-018-4497-4

Bell SS, Chand SS, Tory KJ, Turville C, Ye H (2019b) Eastern North Pacific tropical cyclone activity in historical and future CMIP5

experiments: assessment with a model-independent tracking scheme. Climate Dyn. https://doi.org/10.1007/S00382-019-04830-0

Bell SS, Chand SS, Camargo SJ, Tory KJ, Turville C, Ye H (2019c) Western North Pacific tropical cyclone tracks in CMIP5 models: assessment using a model-independent detection and tracking scheme. J Clim 32:7191–7208. https://doi.org/10.1175/JCLI-D-18-0785.1

Bell SS, Chand SS, Turville C (2020a) Projected changes in ENSO-driven regional tropical cyclone tracks. Climate Dyn 54:2533–2559

Bell SS, Chand SS, Tory KJ, Ye H, Turville C (2020b) North Indian tropical cyclone activity in CMIP5 experiments: Projections using a model-independent detection scheme. Int J Clim (accepted).

Bi D et al (2012) The ACCESS coupled model: description, control climate and evaluation. Aust Meteor Oceanog J CMIP5 Special Issue, **63**:41–646.

Bister M, Emanuel KA (2002) Low frequency variability of tropical cyclone potential intensity. 1. Interannual to interdecadal variability. J Geophys Res 107:4801. https://doi.org/10.1029/2001JD000776

Camargo SJ, Zebiak SE (2002) Improving the detection and tracking of tropical cyclones in atmospheric general circulation models. Wea Forecasting 17:1152–1162

Chand SS, Tory KJ, Ye H, Walsh KJE (2017) Projected future increase in El Niño-driven tropical cyclone frequency in the Pacific. Nature Clim Change 7:123–127. https://doi.org/10.1038/nclimate3181

Collier MA et al. (2011) The CSIRO-Mk3.6.0 Atmosphere-Ocean GCM: participation in CMIP5 and data publication. In: 19th International congress on modelling and simulation, Perth, Australia, 12–16 December 2011 https://mssanz.org.au/modsim2011.

Dixon RD, Daloz AS, Vimont DJ (2017) Saharan heat low biases in CMIP5 models. J Clim 30:2867–2884

Donner LJ, Coauthors, (2011) The dynamical core, physical parameterizations, and basic simulation characteristics of the atmospheric component AM3 of the GFDL global coupled model CM3. J Clim 24:3484–3519. https://doi.org/10.1175/2011JCLI3955.1

Dufresne J-L, Foujols M-A, Denvil S, Caubel A, Marti O, Olivier A, Balkanski Y, Bekki S, Bellenger H, Benshila R, Bony S, Bopp L, Braconnot P, Brockmann P, Cadule P, Cheruy F, Codron F, Cozic A, Cugnet D, De Noblet N, Duvel J-P, Ethe FL, Fichefet T, Flavoni S, Friedlingstein P, Grandpeix J-Y, Guez L, Guilyardi E, Hauglustaine D, Hourdin F, Idelkadi A, Ghattas J, Joussaume S, Kageyama M, Krinner G, Labetoulle S, Lahellec A, Lefebvre M, Lefevre F, Levy C, Zhanbin Li, Lloyd J, Lott F, Madec G, Mancip M, Marchand M, Masson S, Meurdesoif Y, Mignot J, Musat I, Parouty S, Polcher J, Rio C, Schulz M, Swingedouw D, Szopa S, Claude T, Terray P, Viovy N, Vuichard N (2013) Climate change projections using the IPSL-CM5 earth system model: from CMIP3 to CMIP5. Clim Dyn 40(9–10):2123–2165. https://doi.org/10.1007/s00382-012-1636-1

Dunkerton TJ, Montgomery MT, Wang Z (2009) Tropical cyclogenesis in a tropical wave critical layer: easterly waves. Atmos Chem Phys 9:5587–5646

Gent PR, Coauthors, (2011) The community climate system model version 4. J Clim Special Collections 24:4973–4991

Jones CD, Coauthors, (2011) The HadGEM2-ES implementation of CMIP5 centennial simulations. Geosci Model Dev 4:543–570

Knapp KR, Kruk MC, Levinson DH, Diamond HJ, Neumann CJ (2010) The International best track archieve for climate stewardship (IBTrACS) unifying tropical cyclone data. Bull Amer Meteor Soc 91:363–376

Knutson TR, McBride JL, Chan J-C, Emanuel K, Holland G, Landsea C, Held I, Kossin JP, Srivastava AK, Sugi M (2010) Tropical cyclones and climate change. Nat Geosci 3:157–163

Knutson T, Camargo SJ, Chan JCL, Emanuel K, Ho C-H, Kossin J, et al (2019) Tropical cyclones and climate change assessment: part II. projected response to anthropogenic warming. Bull Am Meteorol Soc, 0(0), null.https://doi.org/10.1175/BAMS-D-18-0194.1

Knutti R, Masson D, Gettelman A (2013) Climate model genealogy: generation CMIP5 and how we got there. Geophys Res Lett 40:1194–1199

Li G, Xie S-P (2014) Tropical biases in CMIP5 multimodel ensemble: the excessive equatorial Pacific cold tngue and double ITCZ problems. J Clim 27:1765–1780. https://doi.org/10.1175/JCLI-D-13-00337.1

Martin ER, Thorncroft C (2015) Representation of African easterly waves in CMIP5 models. J Clim 28:7702–7715

Patricola CM, Saravanan R, Chang P (2018) The response of Atlantic tropical cyclones to suppression of African easterly waves. Geophys Res Lett 45:471–479. https://doi.org/10.1002/2017GL076081

Sheffield J, Camargo SJ, Rong Fu, Qi Hu, Jiang X, Johnson N, Karnauskas KB, Kim ST, Kinter J, Kumar S, Langenbrunner B, Maloney E, Mariotti A, Meyerson JE, David Neelin J, Nigam S, Pan Z, Ruiz-Barradas A, Seager R, Serra YL, Sun D-Z, Wang C, Xie S-P, Jin-Yi Yu, Zhang T, Zhao M (2013) North American climate in CMIP5 experiments. Part II: evaluation of historical simulations of intraseasonal to decadal variability. J Climate 26:9247–9290

Taylor KE, Stouffer RJ, Meehl GA (2012) An overview of CMIP5 and the experiment design. Bull Am Meteor Soc 93:485–498

Tory KJ, Dare RA, Davidson NE, McBride JL, Chand SS (2013a) The importance of low-deformation vorticity in tropical cyclone formation. Atmos Chem Phys 13:2115–2132

Tory KJ, Chand SS, Dare RA, McBride JL (2013b) The development and assessment of a model-, grid- and basin independent tropical cyclone detection scheme. J Clim 26:5493–5507

Tory KJ, Chand SS, Dare RA, McBride JL (2013c) An assessment of a model-independent tropical cyclone detection procedure in selected CMIP3 global climate models. J Clim 26:5508–5522

Tory KJ, Chand SS, McBride JL, Ye H, Dare RA (2013d) Projected changes in late 21st century tropical cyclone frequency in thirteen coupled climate models from the coupled model intercomparison project phase 5, J Clim 26:9946–9959

Tory KJ, Chand S, McBride J, Ye H, Dare R (2014) Projected changes in late 21st century tropical cyclone frequency in CMIP5 models. In: Proc. 31st Conference on hurricanes and tropical meteorology, 30 March–4 April 2014, San Diego, CA, American Meteorological Society.

Tory KJ, Dare RA (2015) Sea surface temperature thresholds for tropical cyclone formation. J Clim 28:8171–8183

Tory KJ, Ye H, Dare RA (2018) Understanding the geographic distribution of tropical cyclone formation for applications in climate models. Climate Dyn 50:2489–2512. https://doi.org/10.1007/s00382-017-3752-4

Voldoire A, Coauthors, (2012) The CNRM-CM5.1 global climate model: description and basic evaluation. Clim Dyn 40:2091–2121

Walsh KJE, McBride JL, Klotzbach PJ, Balachandran S, Camargo SJ, Holland G, Knutson TR, Kossin JP, Lee T-C, Sobel A, Sugi M (2015) Tropical cyclones and climate change. WIREs Clim Change DOI: 10.1002/WCC.371

Wang C, Wu L (2018) Projection of North Pacific tropical upper-tropospheric trough in CMIP5 models: implications for changes in tropical cyclone formation locations. J Clim 31:761–774. https://doi.org/10.1175/JCLI-D-17-0292.1

Watanabe S, Hajima T, Sudo K, Nagashima T, Takemura T, Okajima H, Nozawa T, Kawase H, Abe M, Yokohata T, Ise T, Sato H, Kato E, Takata K, Emori S, Kawamiya M (2011) MIROC-ESM 2010: Model description and basic results of CMIP5-20c3m

experiments. Geosci Model Dev 4:845–872. https://doi.org/10.5194/gmd-4-845-2011

Wu T et al (2014) An overview of BCC climate system model development and application for climate change studies. J Meteor Res 28:34–56. https://doi.org/10.1007/s13351-014-3041-7

Yukimoto S, Adachi Y, Hosaka M, Sakami T, Yoshimura H, Hirabara M, Tanaka TY, Shindo E, Tsujino H, Deushi M, Mizuta R, Yabu S, Obata A, Nakano H, Koshiro T, Ose T, Kitoh A (2012) A new global climate model of the Meteorological Research Institute: MRI-CGCM3—model description and basic performance. J Met Soc Japan 90:23–64. https://doi.org/10.2151/jmsj.2012-A02

Zheng X-T, Xie S-P, Du Y, Liu L, Huang G, Liu Q (2013) Indian Ocean Dipole response to global warming in the CMIP5 multimodel ensemble. J Clim 26:6067–6080. https://doi.org/10.1175/JCLI-D-12-00638.1

Zhou TJ, Wang B, Yu YQ, Liu YM, Zheng WP, Li LJ, Wu B, Lin PF, Guo Z, and Zhang WX (2018) The FGOALS climate system model as a modeling tool for supporting climate sciences: an overview. Earth Planet Phys 2(4):276–291. https://doi.org/10.26464/epp2018026

Publisher's Note Springer Nature remains neutral with regard to jurisdictional claims in published maps and institutional affiliations.